Cosmic Bulk Flows: Measuring the Geometrical Effects

Shreeya Nadgowda

University of Potsdam

A thesis submitted for the degree of
Master of Science
in Astrophysics

Supervised by:
Dr. Noam Libeskind
Prof. Dr. Philipp Richter

Statement of originality

I hereby declare that the submitted Master's thesis is my work and that, to the best of my knowledge, it contains no sources or resources other than the ones mentioned and acknowledged. During the wring the writing of the thesis, I indicated all quotes, citations, and references that were taken from published or unpublished publications, such as books, journals, academic articles, newspapers, reports, etc. Furthermore, the research described in this thesis is based on work conducted at the Leibniz-Institut für Astrophysik Potsdam (AIP) and no part of this thesis has been submitted elsewhere for any other degree or qualification

Acknowledgements

Zusammenfassung

Die Eigengeschwindigkeiten sind die Geschwindigkeiten von Galaxien relativ zur kosmischen Hintergrundstrahlung (CMB). Der Mittelwert dieser besonderen Geschwindigkeiten bestimmt die Massenströmung auf kosmologischen Skalen. Die Untersuchung der Massenströmung ist ein interessanter Ansatz zum Verständnis des kosmologischen Modells. Wir sehen, wie Beobachtungseffekte die kosmologischen Bulk-Flow-Messungen möglicherweise verfälschen könnten. Bei den meisten Durchmusterungen von Galaxien wird versucht, die Strömung in einer Kugel um den Beobachter herum zu berechnen. Mit Hilfe von MultiDark-Simulationen werden die Auswirkungen von nicht sphärischen Galaxiendurchmusterungskatalogen auf die Messungen des Volumenstroms untersucht. Die Studie zeigt, dass die Unterabtastung verschiedener Durchmusterungsvolumina - von sphärisch-symmetrischen bis hin zu halbkugelförmigen und engkegeligen Durchmusterungen - zu starken Verzerrungen führt. Es besteht eine starke Abhängigkeit der Volumenstrommessungen von den Vermessungsgeometrien. Bei den nicht sphärischen Geometrien wird die Größe des Volumenstroms überschätzt. Daher können die herkömmlichen Methoden zur Schätzung des Volumenstroms die Größe des Volumenstroms überbewerten. Dies könnte auch erklären, warum Volumenstrommessungen Volumenstromgeschwindigkeiten ergeben haben, die höher zu sein scheinen als die von der Λ-CDM-Kosmologie vorhergesagten.

Abstract

The peculiar velocities are the velocities of galaxies relative to the cosmic wave background (CMB) radiation. The average of these peculiar velocities determines the bulk flow on cosmological scales. The study of bulk flow is an interesting probe to understand the cosmological model. We see how observational effects could possibly bias cosmological bulk flow measurements. In most galaxy surveys bulk flow calculations try to approximate the flow that would occur in a sphere around the observer. Using the MultiDark simulation simulations to study the sampling effects of non-spherical galaxy survey catalogs on the measurements of bulk flow. The study involves shows that strong bias is introduced by undersampling various survey volumes from spherically symmetric, to hemispherical and narrow cone surveys. There is a strong dependence on the bulk flow measurements on the survey geometries. The non-spherical geometries are observed to have an overestimation of the magnitude of the bulk flow. Hence the traditional methods for bulk flow estimation can overestimate the magnitude of the bulk flow. This might also explain why bulk flow measurements have revealed bulk flow velocities that appear to be higher than those predicted by Λ-CDM cosmology.

Contents

v

List of Tables

Chapter 1

Introduction

1.1 Introduction and motivation

The Copernican revolution placed the Sun at the center of our solar system from the initial earth-centric model. The groundwork for understanding the universe was laid during this European Renaissance. Newton's gravitational law showed us that, objects fall on the Earth for the same reasons as the Earth goes around the Sun. He further stated Kepler's law as a consequence of his own laws of motion combined with the universal law of gravitation. Newton's theory of gravitation laid a framework for the understanding of gravity and its role in the dynamics of the universe. With the basis of Newton's classical physics theories, Einstein developed the general theory of relativity. Although Newton's theory was suppressed by this new understanding of gravity the Newtonian framework of gravity still remains useful.

Einstein's theory suggests that the universe is not static and that matter and energy determine the curvature of space-time (Einstein (1915)). This along with the basis of the Copernican principle was useful for the development of the Friedmann-Lemaître models of the expanding universe. The Friedmann-Lemaître models or Friedmann-Lemaître Robertson-Walker (FLRW) models in the framework of the FLRW metric describe the evolution of the expanding universe (Ellis and van Elst (1999)). The models also assume homogeneity and isotropy of the universe on a large scale.

Even though the universe is expanding in accordance with the FLRW models on average, there are regions where the gravitational force is stronger than the general cosmic expansion. As a result, there is coherent motion of the matter in a particular direction in that region. This coherent motion of galaxies and galaxy clusters contributes to the peculiar velocity component in addition to the overall expansion or Hubble flow. On a large scale, this local deviation from the Hubble flow manifests as the bulk flow (Peter Coles and Francesco Lucchin (2002)).

We can study the distribution of matter on the large scales of the universe with the bulk flows. This indeed helps us to understand the models of structure formation and study the distribution of dark matter. By comparing the properties of the bulk flow with the prediction from the existing models, we can constrain parameters like matter density, energy density, and Hubble constant. The bulk flow provides

information about the local deviation from the uniform Hubble flow to understand the motion of galaxies and galaxy clusters under the influence of gravity. Peculiar velocity plays a central role in the detecting and quantifying the bulk flow. Other methods include the study of the peculiar velocity with the redshift space distortions and with gravitational lensing.

Peculiar velocity can be added or subtracted to the total velocity based on the direction of the motion. The velocity field of the local supercluster was studied by (Han and Mould (1990)) giving the value of 331 ± 41 km/s towards the Virgo Cluster. The studies suggested that there is a bulk motion of the galaxies in the local universe towards the Virgo cluster. The Virgocentric infall (Schechter (1981)) is due to the gravitational pull of the matter towards the cluster, which is actively studied even today. In addition to the peculiar velocity field, the tidal velocity field is also studied by (Lilje (1986)) to obtain better measurements of the cosmic bulk flow. The findings implicated a quadrupolar tidal velocity of ~ 200 km/s in addition to the Virgocentric infall.

The advent of recent galaxy redshift surveys like the Sloan Digital Sky Survey (SDSS) (Howlett (2022)) and 2dF Galaxy Redshift Survey (Colless (2001)) covers vast regions of the sky. This makes the study of the bulk flows more precise in measurements. These surveys reduce the effects of redshift space like 'Fingers of God' and isolate the bulk flow measurements. The peculiar velocity catalogs of galaxies based on the Tully-Fisher relation like Cosmicflows are useful for these measurements (Tully (2016)).

The peculiar velocity readings are subject to a few observational constraints, which act as a source of inaccuracy. The galaxy redshift surveys require accurate measurements of the redshift effect. The CMB dipole pattern created due to the relative motion of the Earth relative to the CMB frame has to be subtracted accurately. Observational data noise and systematic instrument errors can introduce uncertainty in the measurements. If there is a selection bias in the sampling of the data such as a survey of particular types of galaxies can impact the measurements. Also, observations being limited by volume introduce statistical variations on a large scale (Wojtak (2014)). The number and location of the detected galaxies in the sky have an impact on how precisely the peculiar velocity measurements are made.

Large-scale surveys with complete sky-covered measurements are robust for the prediction of the bulk flow. However, the survey geometries are non-spherical and do not cover the entire sky. As the galaxy distribution in the universe is not uniform on the local scales, the cosmic web includes the presence of voids, galaxy clusters, and superclusters. This creates empty regions in space where no data can be measured. The presence of the zone of avoidance in the line of sight of observational data can also constrain our measurements. Typically, calculations of bulk flow try to approximate the flow that would occur in a sphere around the observer. This introduces the undersampling effects in the bulk flow measurements. The biases due to this sampling effect are reflected in the overall bulk flow measurements (**?**).

For this thesis, we are particularly interested in the observational effects on the bulk flow measurements and the biases introduced due to these peculiar velocity

measurements. We study the case for the non-spherical survey geometry which introduces the undersampling of velocity distributions. The results could help to explain why several bulk flow observations have revealed bulk flow velocities that appear higher than those predicted by conventional ΛCDM cosmologies. For comparing bulk flows to cosmological models, we use a different method where the theoretical prediction for observation of a bulk flow is subjected to the geometry and sampling rate of that survey.

1.2 Big Bang Model

1.2.1 Cosmological Principle:

Copernican principle states that the Earth is not in a central, specially favored position in the universe. By this principle, it is implicit that the laws of physics apply uniformly throughout the universe. This has been instrumental in the development of different theories in different contexts like the Cosmological principle or the mediocrity principle. One of the profound confirmations of the Copernican principle was by Edwin Hubble. His observations based on the redshift of galaxies suggested that the galaxies are receding away from us (Hubble (1929)). He demonstrated the lack of centrality when the observations were being made, further supporting the idea that all galaxies are moving apart from one another.

The Copernican principle is the cornerstone of our understanding of the universe. The principle is a philosophical and observation stance that addresses the absence of a privileged observer in the universe. Although it does not provide information about the universe and its large-scale structure, it only emphasizes that the universe must have similar properties on a larger scale regardless of the location. Hence the cosmological principle proves to be useful as an extension of the Copernican principle.

The cosmological principle is also the basis of our standard cosmological model today. The principle states that on sufficiently larger scales the universe is both isotropic and homogeneous. By homogeneity, it is meant that, on sufficiently large volumes the matter distribution in the universe is uniform. In other words, any point in space can be chosen as an origin for a frame of reference. Hence homogeneity is the translation invariance of fields of interest. According to the large scale surveys such as SDSS the galaxy distribution in the universe is homogenous at length scales greater than $70h^{-1}Mpc$ (Sarkar et al. (2009)). Isotropy means that the properties of the universe remain the same regardless of the direction in which they are measured. This suggests that we can orient our frame of reference in any direction, and the properties remain the same. Therefore isotropy is related to rotational invariance. The Copernican principle is an additional assumption in favor of isotropy. For scalar quantities homogeneity implies isotropy. The Cosmological Principle is empirically supported by observational data. The mathematical framework for the cosmological principle is also given by the Friedmann-Lemaître-Robertson-Walker (FLRW) metric.

1.2.2 The Robertson-Walker metric

Taking the assumptions of isotropy and homogeneity on larger scales the average evolution of the universe is governed by the metric called Friedmann-Lemaître-Robertson-Walker (FLRW) metric or Robertson-Walker (RW) metric. For simple calculations, we assume the existence of a coordinate system for the universe by taking the t as the time coordinate and, ω, θ, and ϕ as radial, polar, and azimuthal space coordinates. The line element in this homogeneous and isotropic universe is given by,

$$ds^2 = c^2 dt^2 - a^2(t)[d\omega^2 + F_K^2(\omega)(d\theta^2 + \sin^2\theta d\phi^2)] \qquad (1.1)$$

We assume that space-time is filled with fluid hence the ω, θ, and ϕ are the comoving coordinates of the fluid element, and t is the proper time of the comoving clock in such an element. $f_k(\omega)$ can be trigonometric, hyperbolic or linear in ω. The solutions are given as,

$$f_k(\omega) = \begin{cases} \frac{1}{\sqrt{k}}\sin(\sqrt{k}\omega), & (\text{k} > 0) \\ \omega, & (\text{k=0}) \\ \frac{1}{\sqrt{-k}}\sinh(\sqrt{-k}\omega), & (k < 0) \end{cases}$$

For complete proof see (D'Inverno (1992)). Here k is the curvature constant which is related to the geometry of the three-dimensional spatial hypersurface in a way that: $k < 0$ is the geometry of an open universe, $k=0$ is the flat universe and $k > 0$ gives the geometry of a closed universe with k having units of length.

The ds^2 in the equation (1.1) represents the spacetime interval, which is a measure of the separation between two events in spacetime, c is the speed of light, dt represents the differential time, which measures the time interval between two events, $a(t)$ is the scale factor, which characterizes the expansion of the universe as a function of time. As the universe expands, $a(t)$ increases. In terms of spherical polar coordinates, where $r \equiv f_k(\omega)$, dr^2 represents the differential spatial distance, which measures the spatial interval between two points in the universe. The metric takes the form,

$$ds^2 = c^2 dt^2 - a(t)^2 \left[\frac{dr^2}{1 - Kr^2} + r^2(d\theta^2 + \sin^2\theta d\phi^2) \right] \qquad (1.3)$$

The FLRW metric is tailored to describe the universe which is isotropic and homogeneous. By applying this metric to Einstein's field equation we can solve for the evolution of the scale factor $a(t)$.

1.2.3 Friedmann Equations:

Space-time is a four-dimensional manifold, according to General Relativity with its metric tensor $g_{\mu\nu}$ being a dynamical field. The dynamics of this field are given by

Einstein's field equation.

$$G_{\mu\nu} \equiv R_{\mu\nu} - \frac{1}{2}Rg_{\mu\nu} - \Lambda g_{\mu\nu} = \frac{8\pi G}{c^4}T_{\mu\nu} \tag{1.4}$$

The terms $T_{\mu\nu}$ which is the energy-momentum tensor and the Λ, cosmological constant help to understand the dark energy or the expansion of the universe.

As mentioned above we have assumed the space-time to be filled with the perfect fluid of pressure p and density ρ and it is considered to have the four-velocity u_μ. Taking into account the expansion of the universe and the metric, in the end, we get 2 differential equations for $a(t)$ from Einstein's equation.

$$(\frac{\dot{a}}{a})^2 = \frac{8\pi G}{3}\rho - \frac{k}{a^2} \tag{1.5}$$

$$(\frac{\ddot{a}}{a}) = -\frac{4\pi G}{3}(\rho + 3p) \tag{1.6}$$

These are known as the Friedmann equations (Friedman (1922)). The term $(\frac{\dot{a}}{a})$ is called the Hubble parameter (H) which measures the expansion rate of the universe. The current value of this parameter is called the Hubble constant whose value is given as $H_0 = 100$ h km $s^{-1}Mpc^{-1}$ and the uncertainty is expressed as the best value of h = 0.72 ± 0.08 (Freedman et al. (2001)).

1.2.4   Redshift

A more relatable variable to understand the scale factor of the universe is redshift. The cosmic redshift z uses geometrical and observational considerations to explain the expansion of the universe predicted by the Friedmann equations previously. Redshift of a luminous source such as a galaxy is given by,

$$z = \frac{\lambda_0 - \lambda_e}{\lambda_e} \tag{1.7}$$

Here λ_e is the wavelength of radiation emitted from the source observed at O (which can be the origin of our coordinate system) at time t_e or initial time. The source is moving with the expansion of the universe and is at a comoving coordinate r. The wavelength of radiation observed by the observer is λ_0 at the time t_0.

The observation and emission time of the light source is given as $t_0'=t_0+ \delta t_0$ and $t_e'=t_e+ \delta t_e$ respectively. The source and the observer both are in the comoving coordinates hence for unchanging $f(r)$ we get,

$$\int_{t_e}^{t_0} \frac{cdt}{a(t)} = \int_0^r \frac{dr}{(1-kr^2)^{1/2}} = f(r) \tag{1.8}$$

The observation and emission time of the light source is given as $t_0'=t_0+ \delta t_0$ and $t_e'=t_e+ \delta t_e$ respectively. The source and the observer both are in the comoving coordinates hence for unchanging $f(r)$ we get,

$$\int_{t_0'}^{t'} \frac{cdt}{a(t)} = f(r) \tag{1.9}$$

If δt and δt_0 are very small we can say from the above equation that,

$$\frac{\delta t_0}{a_0} = \frac{\delta t}{a} \tag{1.10}$$

But we know that $\delta t = \frac{1}{\nu_e}$ and $\delta t_0 = \frac{1}{\nu_0}$ and the frequency indeed can be shown as $\nu_0 = 1/\lambda_0$, $\nu_e = 1/\lambda_e$ hence we can say,

$$\frac{a}{\lambda_e} = \frac{a_0}{\lambda_0} \tag{1.11}$$

this is written as

$$1 + z = \frac{a_0}{a} \tag{1.12}$$

1.2.5 Cosmological Distances:

The spacetimes of non-euclidean geometries and arbitrary shapes have different distance and time measurements. The distance does not simply mean connecting two points at the same instant in time. There are mainly two reasons for this one is the finite speed of light takes time to connect the points and the second is simultaneity is dependent upon relative motion in two points.

There are three different distance scales that are considered proper distance, comoving distance, luminosity distance, and angular diameter distance. These distances are the unique way to connect the scale factor a(t) to the coordinate time. For the purpose of this thesis, the proper distance and the comoving distance are important

Proper Distance: The distance measured by the time required for light to reach from the source to the observer is called the proper distance D_{prop}. Hence it is given as

$$dD_{prop}(z_1, z_2) = -cdt = -c\frac{da}{\dot{a}} \tag{1.13}$$

the negative sign indicates that the D_{prop} should increase away from the observer while t and a(t) should increase towards the observer.

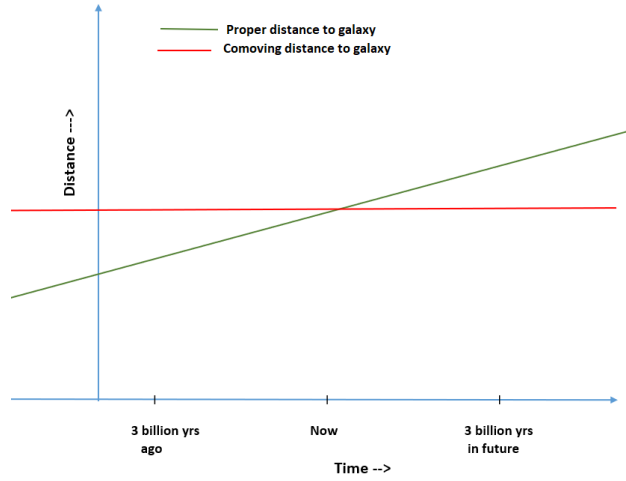$$D_{prop} = c \int_{a(z_2)}^{a(z_1)} \frac{da}{\dot{a}} \tag{1.14}$$

Figure 1.1: The image shows proper and comoving distances as a function of time. As the universe expands the proper distance between galaxies increases but the comoving distance remains the same.

Comoving Distance: The comoving distance D_{com} is the distance between the world lines of the source and observer comoving on spatial hypersurface at a constant time (t= const). Hence this is the coordinate distance between the source and the observer which can be given by,

$$D_{com}(z_1, z_2) = c \int_{a(z_2)}^{a(z_1)} \frac{da}{a\dot{a}} \tag{1.15}$$

1.2.6 Epochs of the Universe:

The evolution of the universe had three epochs in which the evolution was dominated by one of the three components matter, radiation or vacuum energy.

Radiation dominated era: In the early universe radiation dominated. The universe was filled with non-degenerate ultra-relativistic gas in thermal equilibrium. The density contribution varied as $\rho_r \propto a^{-4}$. There is an additional 'a' along with the dilution effect for the expansion for the redshift of the photon momentum.

Matter Dominated era: Before non-relativistic matter started dominating there was a matter-radiation equality era where the energy density of ordinary and relativistic matter was equal.

$$a_{eq} = \frac{\rho_r}{\rho_m} \tag{1.16}$$

After this, the non-relativistic matter starts dominating. Here we assume the universe is filled with the pressureless fluid which is a good approximation for the non-relativistic gas, $p << \rho c^2$. The density dilutes directly as the proper volume expands which is given by $\rho_m \propto a^{-3}$. This is the conservation law of total energy for a comoving frame.

Domination of Cosmological Constant: This can be described by the fluid with negative pressure. From the matter domination epoch to the Λ-dominated

7

epoch occured at,

$$a_{eq,\Lambda} = \sqrt[3]{\frac{\rho_m}{\rho_\Lambda}} \tag{1.17}$$

The density of the flat universe without taking into consideration the cosmological constant is called as the critical density,

$$\rho_{cr} \equiv \frac{3H_0^2}{8\pi G} \tag{1.18}$$

This quantity helps us to define the dimensionless density parameters as,

$$\Omega_f \equiv \left(\frac{\rho_f}{\rho_{cr}}\right)_{today} \tag{1.19}$$

Hence,

$$\Omega_{m(a)} = \frac{8\pi G}{3H^2(a)} \frac{\rho_m(t_0)}{a^3} \tag{1.20}$$

and

$$\Omega_{\Lambda(a)} = \frac{\Lambda c^2}{3H^2(a)} \tag{1.21}$$

1.3 Gravitational Evolution

1.3.1 Linear Eulerian Perturbation Theory:

The matter in our universe is not distributed homogeneously at all scales. The small density perturbations were seeded in the inflation period in an otherwise homogeneous universe. Due to gravity these perturbations grew in amplitude and led to the formation of the structures that we see today in the Universe. Eulerian perturbation theory is the most used theory to study the formation and evolution of the structure. The spatial and time dependence of velocity and density field is studied through this theory. The Eulerian perturbation theory is particularly useful in early times and at large scales where the overdensity is not very large. But for high-density contrast, we take into consideration theories like spherical collapse or we resort to N-body simulations for highly non-linear scales.

At large scales, the dynamics of the universe are mostly governed by dark matter. Hence we can assume the universe to be a continuous fluid. We consider the Newtonian limit of the equation of motion with small perturbations. As the motions of cold matter in the universe are non-relativistic ($v << c$). The description of the full evolution of the density, velocity, and gravitational field is possible with the equations of motion. To describe the evolution of this fluid three equations are used, the continuity equation, the Euler equation, and the Poisson equation.

$$\partial_t \rho + \nabla_x \cdot \rho v = 0 \quad \text{continuity equation} \tag{1.22}$$

$$\partial_t v + (v \cdot \nabla_x)v + \frac{1}{\rho}(\nabla_x)p + \nabla_x \Phi = 0 \quad \text{Euler equation} \tag{1.23}$$

$$\nabla_x^2 \Phi - 4\pi G\rho = 0 \quad \text{Poisson equation} \tag{1.24}$$

The framework of the perturbation theory assumes that gravity is the only agent responsible for the growth of the structure and inhomogeneity. The pressure forces are considered to be negligible. Taking the FLRW metric for flat space-time ($k = 0$) ((1.3)) and including the small perturbations,

$$\rho \equiv \bar{\rho}[1 + \delta] \tag{1.25}$$

$$v = u + H$$

(1.26)

$$\phi = \bar{\phi} + \Phi \tag{1.27}$$

The notations used are as follows,

symbol	meaning	comments
$\bar{\rho}$	average density	
δ	overdensity field	$\delta = \frac{\rho}{\bar{\rho}} - 1$
ρ	density field	
u	peculiar velocity field	
ϕ	gravitational potential	
Ω_m	density parameter	equation (1.20)
$\vec{x}$	comoving position in real space	

Table 1.1: Notations used in this thesis

The total quantities with perturbation give (Bernardeau et al. (2002)):

$$\partial_t \delta = \nabla_x \cdot [(1 + \delta)u] \quad \text{continuity equation} \tag{1.28}$$

$$\partial_t u + H(t)u + (u \cdot \nabla_x)u = -\nabla_x \Phi \quad \text{Euler equation} \tag{1.29}$$

$$\nabla_x^2 \Phi = \frac{3}{2}\Omega_m(t)H^2(t)\delta \quad \text{Poisson equation} \tag{1.30}$$

Here the dependence of δ, u, Φ on ($\vec{x}$,t) is suppressed in the notations. We can then track the development of small fluctuations by linearizing the equations above and ignoring all the higher-order terms. Combining with the Poisson equation,

$$\partial_t \delta + \theta = 0 \tag{1.31}$$

$$\partial_t \delta + H(t)\theta = -\frac{3}{2}\Omega_m(t)H^2(t)\delta \tag{1.32}$$

Where $\theta = \nabla \cdot u(x,t)$. As the initial vorticity decays with time, we assume no vorticity $\nabla \times u = 0$. Combining the equations (1.31) and (1.32) to get,

$$\partial_t^2 \delta + H(t)\partial_t \delta - \frac{3}{2}\Omega_m H^2(t)\delta = 0 \tag{1.33}$$

Which has the general solution of the form,

$$\delta(x,t) = A(x)D_1^{(+)} + B(x)D_1^{(-)} \qquad (1.34)$$

As we want to study the growth of the structure we consider only growing modes and not the decaying ones. Hence taking only the first term on the right-hand side. The linear theory is valid for the density and the velocity perturbations that are very small. For such cases, the second and higher-order terms are negligible and can be discarded.

1.3.2   Dynamics of the structure formation:

We study the inhomogeneity to understand exactly when and how the universe started to depart from the initial uniform density. This can be done by studying the matter in the universe and its evolution due to interaction with the self-gravity. Linear solution of the behavior of matter discussed in the last section can be obtained by taking into account the density perturbations.

$$1 + \delta(x) = \frac{\rho(\vec{x})}{\bar{\rho}} \qquad (1.35)$$

These density perturbations influence the structure formation in the universe. To study these perturbations we consider the fundamental equations governing the fluid motion otherwise called equations of motion from the last section equations (1.31), (1.32), (1.33). There are mainly two ways to introduce perturbations in these equations. The perturbations can be introduced by changes in uniform density by compression or expansion of the volume adiabatically, these are called adiabatic perturbations. The matter density and the radiation density are affected in different ways. The other mode of perturbation is called isocurvature perturbation. Here the entropy density is perturbed and not the energy density so the total density remains homogeneous. The isocurvature perturbations to the radiation are constant. The linear adiabatic perturbations are important for the purpose of understanding the density fluctuations which scale with time as,

$$\delta = \begin{cases} a(t)^2 & \text{(radiation domination)} \\ a(t) & \text{(matter domination)} \end{cases}$$

The equations are given in the Eulerian coordinates for the particles in the motion and the proper length units are used, the Hubble expansion is also taken into consideration. Gravitation causes a non-uniform distribution of the particles to grow more and more irregularly with time. Hence the matter undergoes displacement with respect to the uniformly expanding background universe. The displacements are the most direct ways of identifying the inhomogeneity. Hence we transform the perturbed equation to comoving units. The transformations for position and

peculiar velocity are,

$$x(t) = a(t)r(t) \tag{1.37}$$

$$\delta v(t) = a(t)u(t) \tag{1.38}$$

We can say that the comoving peculiar velocity is just the time derivative of the comoving coordinate r which is given by,

$$\dot{x} = \dot{a}r + a\dot{r} = Hx + a\dot{r} \tag{1.39}$$

Deviation from the Hubble flow hence is the probe for the inhomogeneity which can be studied through the peculiar velocity.

1.4   Bulk Flows:

The FLRW models incorporate the effects of gravity, which are responsible for the formation of cosmic structures such as galaxy clusters, superclusters, and filaments. These structures are not distributed uniformly, and their gravitational interactions can result in peculiar velocities for galaxies within them. Peculiar velocities are the velocities of galaxies relative to the cosmic microwave background (CMB) radiation and can contribute to bulk flows.

1.4.1   Velocity Perturbations:

The equations of motion are defined in the last section. We have the solutions for the δ density perturbations and from there we can determine the velocity fields and gravitational potential field as well in terms of comoving coordinates. As we have seen before $\nabla \times u = 0$ hence the velocity field is irrotational. We can determine the velocity field as a gradient of some velocity potential (Φ_u),

$$u = -\frac{\Phi_u}{a} \tag{1.40}$$

From the peculiar velocity, we can determine the peculiar gravitational acceleration as,

$$g = -\frac{\Phi}{a} \tag{1.41}$$

From the Poisson equation we can say that,

$$\nabla^2 \Phi_v = H f a^2 \delta \tag{1.42}$$

This gives us the relation between the gravitational potential and the velocity potential as,

$$\Phi = \frac{3\Omega H}{2f} \Phi_v \tag{1.43}$$

And hence we can say that,

$$u = \frac{2f}{3\Omega H}g \tag{1.44}$$

This tells us that regardless of the Ω the gravitational acceleration and the velocity will remain in the same direction for linear theory.

We can determine the power spectrum of the field Φ by taking the relation between u and the density perturbation δ. Hence the relation between the density perturbation relation with g can be determined,

$$u(x) = aH\frac{f(\Omega)}{4\pi}\int\frac{\delta(x')(x-x')}{\text{mod }x-x'^3}d^3x' \tag{1.45}$$

Assuming that the power spectrum of the density field is known we can say,

$$P_\Phi(k) = (\frac{3}{2}\Omega H^2 a^2)^2 P(k)k^{-4} \tag{1.46}$$

Hence the velocity power spectrum is,

$$P_u(k) = (aHf)^2 P(k)k^{-2} \tag{1.47}$$

The velocity field is a vector so the power spectrum includes all three components of the u. The power spectrum is useful to determine all the statistical properties of 'u' assuming that δ is a Gaussian random field.

1.4.2 Velocity Correlations:

Now taking things from Fourier space to real space and determining the properties of u in a statistical manner we take the scalar velocity covariance function as,

$$\epsilon_u(r) = \langle u(x_1) \cdot u(x_2)\rangle \tag{1.48}$$

Here r= $|x_1 - x_2|$. Hence the function can be expressed as,

$$\epsilon_u(r) = \frac{(H_0 f)^2}{2\pi^2}\int p(k)j_0(kr)dk \tag{1.49}$$

Hence we can find the statistical properties of the velocity field. However, there is a problem with such a practice. For a continuous velocity field sampled at random positions in the galaxy catalog all the density distribution is not covered as the galaxies taken only the overdense regions in the space. Hence any practice based on the correlation between the density and the velocity field will result in biased estimates.

1.4.3 Bulk Flows:
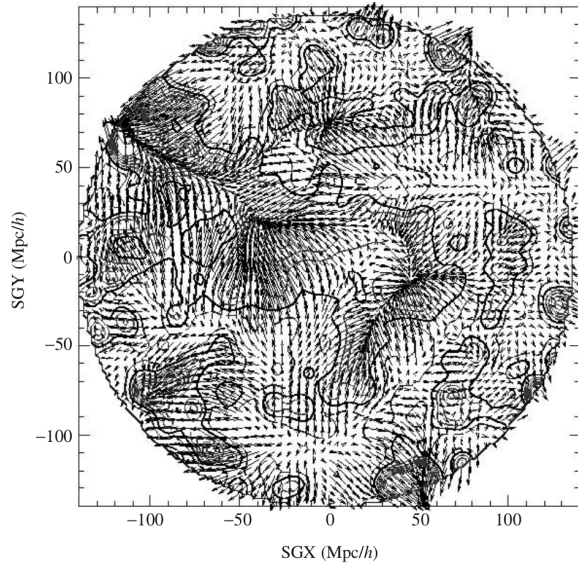
Figure 1.2: The image shows the reconstruction of the density-velocity field using the PSCz redshift catalog. The x and the y axes are supergalactic planes along x and y coordinates respectively. The vector arrows shown are the projection of the velocity field and the contours show lines with similar δ (Peter Coles and Francesco Lucchin (2002))

Bulk flows are one of the simplest ways to study and measure peculiar velocities. Cosmic Bulk Flow is the net motion of matter in a large region. Typically in the galaxy catalogs, this is a large spherical region centered on the observer. The formula for the bulk flow is,

$$V_{BF} = (V_x^2 + V_y^2 + V_z^2)^{1/2} \tag{1.50}$$

The density field is Gaussian and so each component of the velocity field in the above equation is Gaussian. Hence the averaged velocity V will follow the Maxwellian distribution which is given by,

$$P(V)dV = \sqrt{\frac{54}{\pi}}(\frac{V}{\sigma_V})^2 exp[-\frac{3}{2}(\frac{V}{\sigma_V})^2]\frac{dV}{\sigma_V} \tag{1.51}$$

Here V is the filtered velocity which is given by,

$$V(x, R) = \frac{1}{(2\pi)^3} \int \tilde{V}(k)W_V(k, R)exp(-ik \cdot x)dk \tag{1.52}$$

Where $W_V(k, R)$ is a chosen window function. It is chosen according to the construction of the sample of study. We chose the top-hat window function for our sample. From the velocity power spectrum, we can say that,

$$\sigma_V^2(R) = \frac{(H_0 f)^2}{2\pi^2} \int_0^\infty P(k)W_V^2(k, R)dk \tag{1.53}$$

In an ideal isotropic and homogeneous universe the mean bulk flow should be zero. Hence there should not be any deviations from the standard values of the σ.

But we observe the deviation in our measurements. From the equation above we can see that the bulk flow depends on the linear terms of k hence it proves useful in probing the linear regime of P(k). Hence on a large enough scale, we can use the bulk flow as a probe via the predictions of the linear theory.

Chapter 2

Methodology

The standard cosmological model explains the expansion of the universe by cosmological constant and matter density dominated by dark matter. At scales much smaller than the Hubble radius, CDM particles are non-relativistic the equations of motion are with consideration of Newtonian gravity studied with the equations (1.31), (1.32), (1.33). The dynamics of the universe are dominated by gravity on the larger scales, the baryons and the dark matter can be taken as a single pressureless cold fluid. This scenario makes the choice of computer simulations ideal for studying the evolution of such systems because by taking the initial condition and the known laws of physics we can predict the evolution of the system by gravitational interactions alone. These simulations, especially N-body simulations, start from initial conditions that show small fluctuations in the universe's density, these fluctuations are evolved under gravity's influence, resulting in the formation of structures from the smallest scales to the largest observable phenomena. This growth of structures goes from linear to highly nonlinear scales. The $\Lambda-$CDM model is compatible with all the observations of the large-scale structure even at non-linear scales (see Vogelsberger et al. (2016)). But to solve the problem on highly nonlinear scales we can only rely on the computational simulations. Hence, in recent times, simulations have played a critical role in the validation and testing of the $\Lambda-$CDM model as well as the study of the large-scale structure.

In simulations, dark matter is typically modeled as a collection of particles that interact gravitationally, allowing the study of structure formation in a universe. Dark matter is considered collisionless on large scales, this is perfectly suited for simulation using the N-body method. The N-body method models dark matter as a swarm of particles, enabling the study of how gravity alone can structure the universe.

As we collect more observational data through survey missions like (Laureijs (2011), Lavaux and Hudson (2011)), simulations become increasingly vital for making sense of the information we collect. Simulations give comparable results to the real universe's large-scale structure by taking the appropriate models, and accurate initial conditions.

In this section, the method followed for the bulk flow measurements is discussed. It begins with an explanation of the working of N-body simulations, particle mesh

methods, and different footprints used for the measurements of the bulk flow and the motivation behind using the different footprints. The programming language used for the simulations is Python.

2.1 N-body Simulations
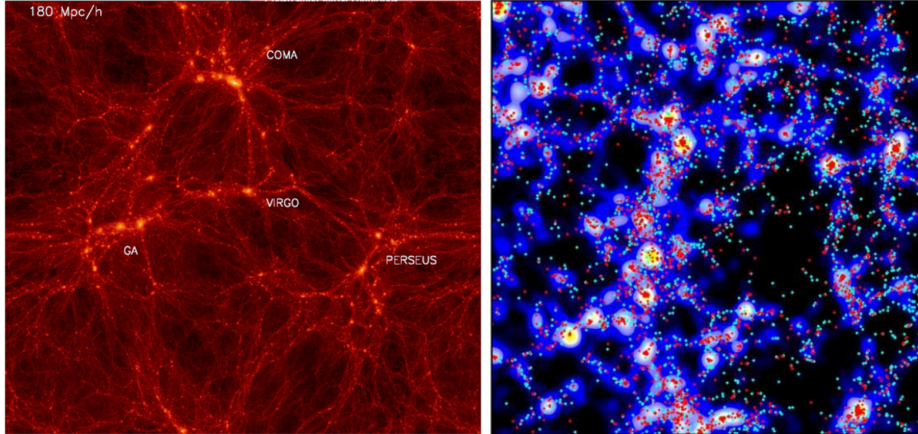
Figure 2.1: N-body simulations of initial fields. The left panel shows the simulations of the local Universe carried out by the CLUES collaboration, where the initial conditions were constrained using the CosmicFlows observations (Tully et al. (2016)). The right panel shows a slice of the density field with thickness of a $200h^{-1}$ Mpc in the ELUCID simulation (Wang et al. (2016)). Here the simulated dark matter is shown in black-blue color, and red/cyan shows the locations of galaxies

Since gravity is the only agent assumed to be responsible for the formation of density fluctuation at large scales, the collisionless limit remains valid for large cosmological scales ($\sim 10^{22}$m). We are considering a large number of particles, to describe the motion of these particles we consider the phase-space distribution function of particles in phase-space over time. For a very large number of particles N $>>$ 1, discreteness effects are considered to be negligible, and collisionless dark matter obeys the Vlasov equation for the distribution function in phase space. The numerical simulations sample this distribution by partitioning phase space into N elementary volumes. Particles are given with initial positions, velocities, and masses. To study the evolution of the universe we consider perturbation around homogenous and isotropic FLRW metric. The particles are taken in the weak-field, non-relativistic, and collisionless limit. Hence Valsov-Poisson (VP) limit describes the equation of motion for the particles. VP describes the evolution of the density in six-dimensional phase space over time. Considering the cosmic time $dt = ad\tau$ the equations of motion solved by the N-body codes are (Angulo and Hahn (2022)),

$$\frac{dX^i}{dt} = \frac{P^i}{m} = \frac{P_i}{ma^2} \text{ and } \frac{dP_i}{dt} = -m\frac{\partial \Phi}{\partial X^i} \tag{2.1}$$

The position and momenta of particles are given by X^i and P^i respectively. Together in the Vlasov-Poisson system, we get,

$$\frac{\partial f_m}{\partial t} + \frac{p_i}{ma^2}\frac{\partial f_m}{\partial x^i} - m\frac{\partial \Phi}{\partial x^i}\frac{\partial f_m}{\partial p_i} \tag{2.2}$$

$$\nabla^2\phi = 4\pi G a^2(\rho - \bar{\rho}) \tag{2.3}$$

$$\rho = \frac{m}{a^3}\int d^3p f_m(\mathbf{x},\mathbf{p},t) \tag{2.4}$$

Equation (2.1) gives the evolution of individual particles. Equations (2.2) is the Vlasov equation that describes the time evolution of the distribution function (f_m), (2.3) is the Poisson equation for the matter density (ρ) and gravitational potential (ϕ). The last equation (2.4) connects the distribution function to the matter density, closing the system. Together the particle's position and momenta can be updated in the equation (2.1) after solving. The discrete trajectories tell us about the evolution of the system.

Various numerical methods have been devised to solve VP dynamics. The N-body approach is the most prominent and important technique today. In the N-body method, a finite number of discrete particles that fairly sample the density field are taken. The simulations are restricted in the finite volume (L^3) with the comoving linear extent L and periodic boundary conditions. Taking the discrete macroscopic particle momenta and locations the phase space distribution is then described along with the infinite set of periodic copies.

2.1.1 Initial Conditions:

The initial conditions in the cosmological N-body simulations are supposed to reproduce the statistical properties of the density field in the early universe. However, this has to be achieved with a limited number of particles which are the tracers of dark matter in the six-dimensional phase space. The widespread choice for mass is the one where all the particles have equal mass. The initial momenta (P_i) and the positions (X_i) of the particles at some initial time (t_0) are the defining initial conditions of the system.

The initial density is generated by introducing perturbation in the uniform grid of particles according to the power spectrum derived from the CMB data. The positions and velocities (or momenta if the mass is the same for all the particles) of the particles are in such a way that they reflect the density field perturbations. For accuracy in calculations, we use Lagrangian perturbation theory or Zel'dovich approximations. After the initial sampling of the particles is determined, the subsequent calculations are done using the equations of motions as described above in section 2.1 to evolve the system.

2.2 Particle Mesh Methods:

The direct method for the N-body simulations with the numerical integrations would require calculations on the order of $\frac{1}{2}N^2$ to evaluate the potential energy of N particles. For a system with many particles these $O(N^2)$ computations are time consuming. Hence to reduce the time complexity many approximate methods have been developed for the purpose of computations.

One of the methods is the particle mesh method. The way particle mesh methods work is as follows:

1. Assign charge/mass to a suitable mesh
2. Solve the potential equation (e.g Poisson's equation (2.3)) on the mesh
3. Calculate the force field on the mesh from the potential
4. Calculate the force on the particle by interpolating the forces on the grid
5. Integrate these forces to get the updated positions and the velocities of the particles
6. Update the time counter

The mass assignment is done using multiple techniques. For the purpose of this thesis, we focused on a particular method called the Cloud-in-Cell method.

2.2.1 Cloud-in-Cell method:

To map the particle masses onto a grid we have used the Clould-in-Cell (CIC) method. To describe the mass distribution the window function is defined as follows.

$$W_{CIC}(x) = \frac{1}{h} \begin{cases} 1 - \frac{|x|}{\Delta x}, & \text{for } |x| < \Delta x \\ 0, & \text{otherwise} \end{cases}$$

Here h is the width, or size of the cell, and $\frac{1}{h}$ is the step size used for calculations. The window function is calculated by integrating the shape function over the volume considered. Δx takes the position of the particle relative to the grid point. The equation gives a non-zero value only if the cloud of the particle overlaps with the grid cell (refer to fig 2.2). Further calculations are carried out only for this volume of overlap. These mass assignment calculations make sure that the total mass in the end is conserved and correctly distributed to the grid points accounting for the position of the particle.
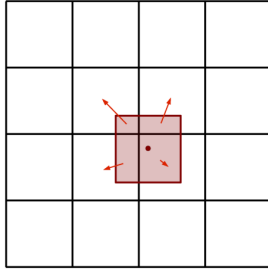
Figure 2.2: The image shows 2D representation of 3D cube considered for the CIC method. The red dot in between represents the particle and the red square around the particle represents the "cloud" around this particle.(credits: Pfrommer (2022))

2.3 Multidark Simulations:
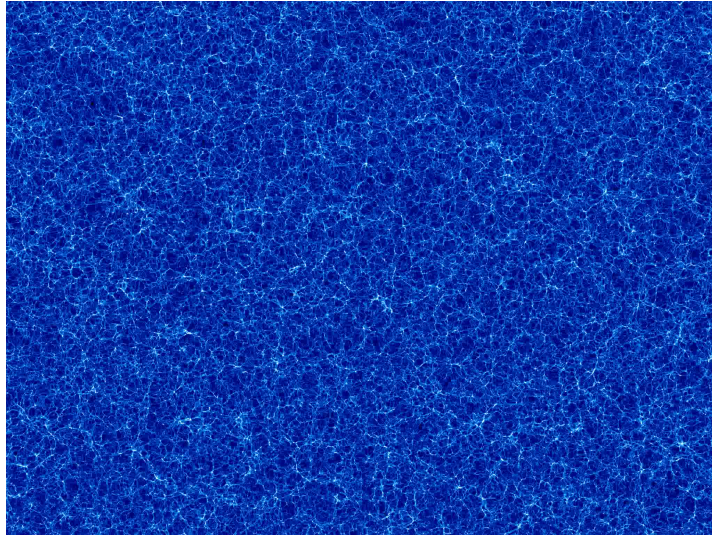
Figure 2.3: A slice of 2.5 Gpc/h box of the BigMDPL simulation (credits: MultiDark project[1])

The simulations in this thesis are performed under the framework of the MultiDark project[1]. These are dark matter-only simulations. The simulations have a box size of 4000 Mpc h^{-1}. The box contains 4096^3 dark matter particles with the mass resolution of 7.9 $\times 10^{10} M_\odot$. To minimize the effect of the cosmic variance for some simulations identical Gaussian fluctuations are chosen. Cosmic variance is very small for simulated volume, but it still needs to be considered when comparing with the observations. These Gaussian fluctuations are taken as the basis to generate the initial conditions generated with Zeldovich approximation at the redshift $z_{init} = 100$. Simulations are done with the Adaptive Refinement Code.

The values for other cosmological parameters are (Klypin et al. (2016)),

---

[1] https://www.multidark.org/

Symbol	Parameter	Values
h	Hubble parameter	0.6777
Ω_Λ	density parameter for dark energy	0.692885
Ω_m	density parameter for matter (dark matter+baryons)	0.307115
Ω_b	density parameter for baryonic matter	0.048206
σ_8	amplitude of mass density fluctuation in 8 Mpc/h sphere	0.8228

Table 2.1: Values of the cosmological parameters used in the MultiDark simulations

2.4 Bulk Flow Calculations:

For the measurement of the bulk flow, a box with dark matter particles only and the size 4 Gpc h^{-1} is taken. The box has comoving coordinates to take into account the expansion of the universe. Mesh with 3 different resolutions are chosen. The grid size or the number of nodes along each dimension are 128, 256, and 512. The higher value indicates a grid with more cells, finer size, and higher spatial resolution. This allows for more precise calculations and minimizes the discreetness effects due to particles in the bulk flow calculations.

We have considered the periodic boundary conditions to create the wrap-around for all the particles especially the ones at the edges of the box. This maintains consistency with the cosmological principle and ensures that the density field used for computing the gravitational potential is smooth and continuous.
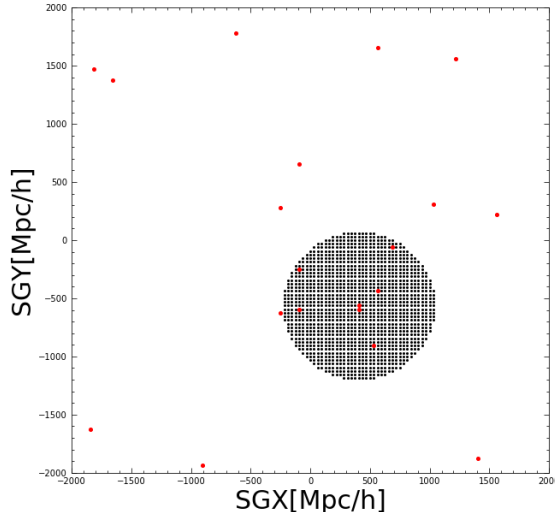
Figure 2.4: The figure shows a slice of the simulation box. The x and y axes give supergalactic coordinate x (SGX) and supergalactic coordinate y (SGY) in Mpc respectively. The slice is 4000 Mpc thick. The red dots show the randomly chosen coordinates for the centers. These are the reference points for further bulk flow calculations. The black spherical area is the sphere chosen for bulk flow calculations.

After defining the initial conditions, the bulk flow is calculated in the following steps:

1. We take the mesh with the desired cell distance or cell per dimension (128^3, 256^3, or 512^3).

2. 1000 points on this mesh are chosen as the observational origins. Random seed is used while generating these origins to ensure reproducibility.

3. Taking these random points as the origins we define the concentric spheres around these origins.

4. The radius of these spherical shells ranges from 40 Mpc $h^{-1} \leq R \leq 440$ Mpc h^{-1}. The sample is chosen in such a way that the calculations cover only 10% of the box each time. This is due to the fact that the calculations beyond this distance do not remain reliable as explained in the section (3.1).

5. We begin with the smallest distance from the center (40 Mpc h^{-1}) and for each iteration, we increase the radii of the sphere in the interval of 10 Mpc h^{-1}.

6. For each concentric sphere we take all the points inside the sphere to calculate the velocity components along each dimension (v_x, v_y, v_z) and then take a mean of velocities along each component and for each sphere.

7. Bulk flow is computed by using the equation (1.50).

8. Eventually the mean and the variance of the bulk flow are calculated.

Different Footprints:

The survey geometries of the velocity field catalogs are not ideal spheres. Hence the ideal spherical calculation models may not always be useful. To get an idea about how the bulk flow calculations are affected by the sampling effects, we consider hemispheres and cones for the calculations of the bulk flow.
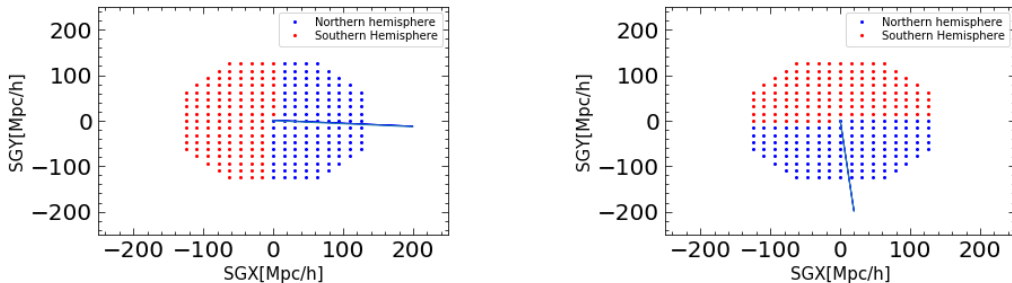
Figure 2.5: The figure shows the 2D representation of hemispheres taken at the Northern and Southern parts of the velocity vector. The x and y axes give supergalactic coordinate x (SGX) and supergalactic coordinate y (SGY) respectively. The light blue line represents the velocity vector. The blue dotted half circle represents the Northern hemisphere taken with respect to the velocity vector and the red dotted circle represents the Southern part of the circle (hemisphere).

For the calculations of the bulk flow in the hemisphere, we take the bulk flow for the whole sphere from previous calculations. The direction of the bulk flow determines the orientation of the hemispheres. The half of the sphere in the direction of the bulk flow is considered the 'northern hemisphere' and the other half which is away is considered the 'southern hemisphere' of the sphere.

We then calculate the bulk flow in hemispheres. The same method of bulk flow calculation is followed for both parts of the sphere to get the velocity components and to get the mean and variance.
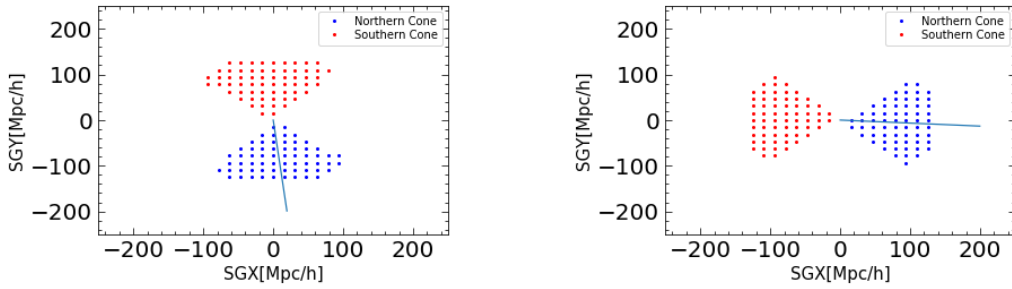
Figure 2.6: The figure shows the 2D representation of cones taken at the Northern and Southern parts of the velocity vector. The x and y axes give supergalactic coordinate x (SGX) and supergalactic coordinate y (SGY) respectively. The light blue line represents the velocity vector. The blue-dotted cone represents the Northern part taken with respect to the velocity vector and the red-dotted part represents the Southern part of the cone

A similar orientation is taken to define the cones of 15° and 30°. The cones are also taken in the direction of the bulk flow and away from the direction of the bulk flow. The bulk flow for each cone is also calculated and the mean is then taken.

To check if the directionality of the bulk flow matters for the calculations we take the cones in a random direction as well. We define a random vector and take the hemisphere and cones around this vector to calculate the bulk flow.

Chapter 3

Results

In this section, I present the characteristics and implications of the bulk flow measurement obtained from simulation results. The chapter consists of discrete sections, each of which focuses on a different geometrical footprint. Section 3.1 incorporates results obtained from ideal spherical geometry. Section 3.2 includes the results for hemispheres. In Section 3.3 the results for small cones are analyzed and lastly, we take into account the results from random sampling in Section 3.4.

The results in this chapter use the 128^3 point grid. This is the most coarse grid size available. Discussions regarding the finer grid with 256^3 point grid are included in Appendix A.1 and results using the halo catalog are in A.2.

3.1   Bulk flow of Whole Sphere:

As discussed earlier the box of size 4000 Mpc/h is considered. There are 4096^3 dark matter particles in the box. To mimic the evolution of density and the velocity field in the actual universe the gravitational evolution of these particles is simulated. The bulk flow calculations are done within the simulated volume. Hence the statistical properties of overdensity (δ) and velocity should also exhibit isotropy and homogeneity on the larger scales. To observe the variance in our measurements, we select 1000 random points in this domain. Taking the variance over such a large volume would approach similar results to that of ensemble variance. These random points act as the origin for the concentric spheres. These randomly selected points can be referred to as observational origins.

The simulations have implemented the periodic boundary conditions. The simulation box is of finite size hence the edges of the box can have an artificial effect as the particles at the edges have fewer neighboring particles. To avoid these effects on the measurements the simulation box wraps around each randomly chosen center.

At first, we calculated the bulk flow for the entire volume in concentric spheres (see figure 3.1). Each curve on this plot represents a random origin and each point on the curve represents a sphere of specific radius. From the figure, we observed that the bulk flow value reaches a maximum of 800 km/s for a very small radius of the sphere. But as the radius of the sphere in our measurements increases, the bulk flow consistently shows a decrease. After the radius of 500 Mpc/h most concentric spheres

show that the bulk flow value reaches to 0. This observation is consistent with the cosmological principle that at sufficiently large scales, the universe is homogeneous and isotropic. This would result in no preference to a specific direction and hence the total bulk flow should be zero.
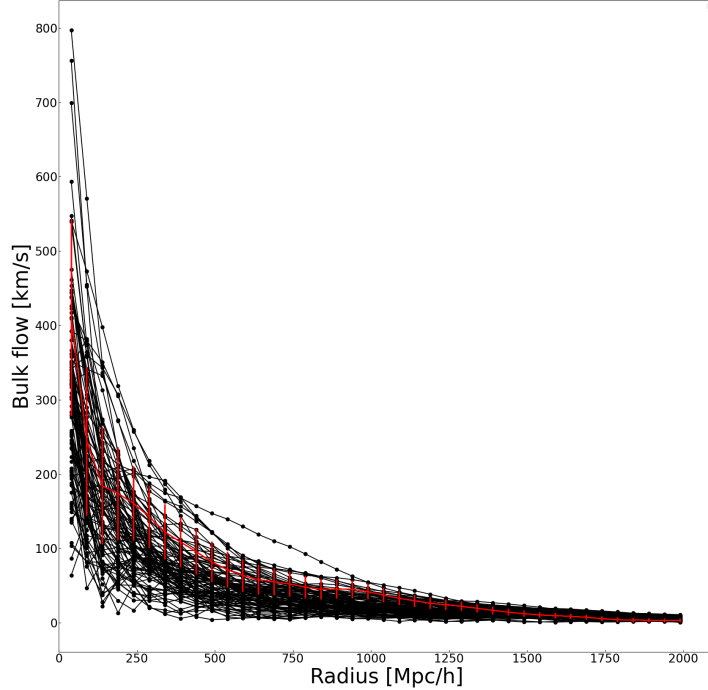
Figure 3.1: The figure gives the Bulk flow calculations in concentric spheres for the entire box of 4000 Mpc/h. The x-axis gives the Radius of the spheres in [Mpc/h] and the y-axis gives the magnitude of the bulk flow in km/s. Each curve represents a randomly chosen center and each dot on the curve represents a concentric sphere. The red dotted line in the middle gives the mean value of the Bulk flow with the variance for all the spheres for all the random centers.

But the scale of interest for this thesis is approximately only till $1/10^{th}$ of the size of the entire box. This choice is based on the suppression effects on the bulk flow measurements, which become more prominent at larger scales. Fig 3.2, shows observed suppression of the bulk flow in the 1 Gpc/h simulation box size compared to the 4 Gpc/h simulation. The velocity values show suppression faster for the smaller box (1 Gpc/h) than the 4 Gpc/h volume. It is seen for both simulations approximately after 10% of the volume the suppression effects are seen. Hence for 1 Gpc/h, it is approximately for a radius of 100 Mpc/h and for 4 Gpc/h we take ~ 400 Mpc/h. As the simulation box mimics the structure and dynamics in the actual universe, within any given simulation box, there is no net movement of the box itself, everything is measured relative to the box. Hence by definition, the box is taken to be a stationary volume. As we approach towards entire volume the bulk flow measurements show suppression due to the unmoving box. Trusting only $1/10^{th}$ of the measurements of the box sizes ensures that the results are least influenced
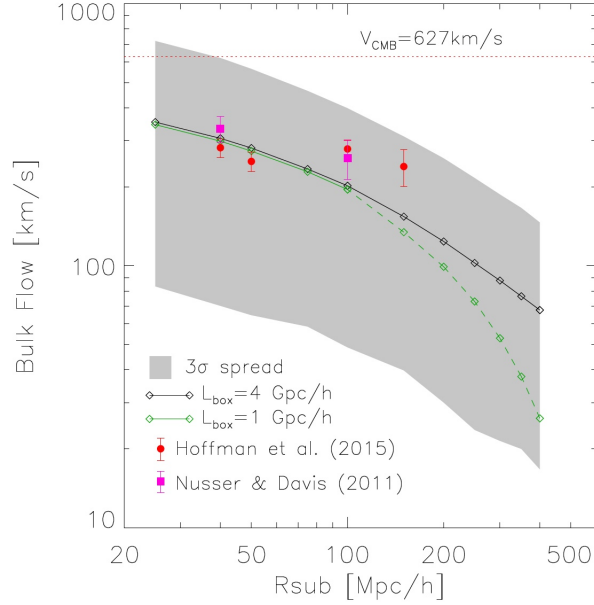
Figure 3.2: The image shows the impact of the simulation scale on the study of bulk flow. The x-axis represents the subsampling into a smaller radius and the y-axis represents the value of the bulk flow. The Green and the black dotted lines show the bulk flow measurement with the box size of 1 Gpc/h and 4 Gpc/h respectively. The grey area represents the 3σ spread over the bulk flow values. The reference bulk flow of CMB is marked with a dashed line above. The red and magenta points with error bars are bulk flow values from other measurements. (Credits: Libeskind private communications)

by the limitations of the box size of the simulations. The local inhomogeneities and anisotropies are still significant and can be analyzed before they vanish into the larger-scale homogeneity. Hence we measure the bulk flow in the till 400 Mpc to cover the 10 % of the box's size. Similar to the previous procedure, 1000 random centers are taken to define the concentric spheres from 40 to 400 Mpc/h in the interval of 20 Mpc/h between each sphere. The results are shown in figure 3.3, each curve represents a chosen center and each dot represents the sphere defined around it. Even though the maximum value of velocity remains similar to the entire box measurements the spread across the various values of velocity is larger here. The red curve in the middle shows the median across all the centers, the error bars around them correspond to 16th and 84th percentile. The velocity field in our measurements is non-gaussian hence median is a more robust measurement and it reflects the maximum sample points from our data. The multitude of lines suggests that even though there is an overall average, an individual case can diverge based on their initial conditions.
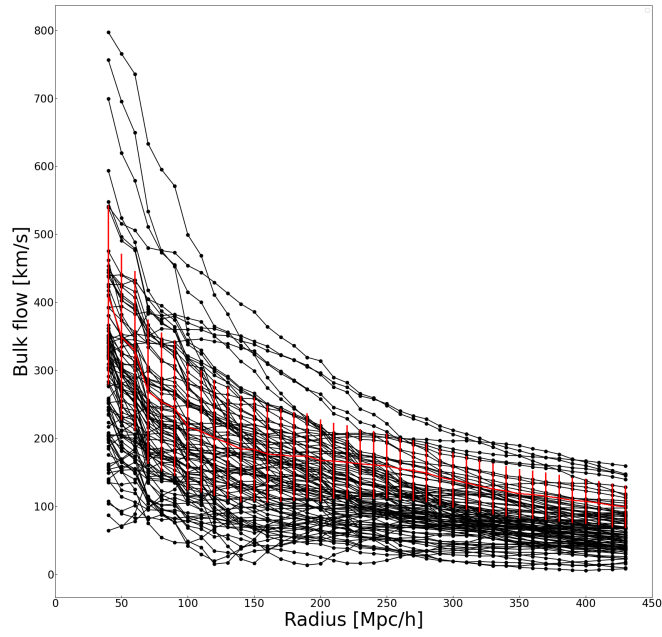
Figure 3.3: The figure gives the Bulk flow calculations for all the concentric spheres at all the random points for the radius of 400 [Mpc/h]. The x and the y axis are the same as the figure 3.1. Each curve represents a randomly chosen center and each dot on the curve represents a sphere. The red dotted line in the middle gives the mean value of the bulk flow for all the spheres for all the random centers.
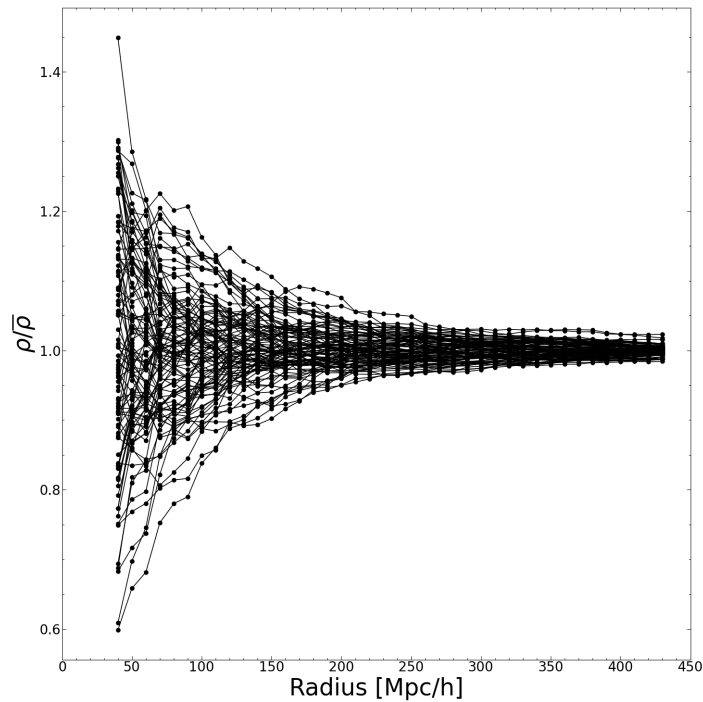
Figure 3.4: The figure shows the density contrast as a function of radius. Here the x-axis is the same as figure 3.1 and the y-axis gives the ratio of the density over the mean density. Each curve and each point on the curve gives a randomly chosen center and a concentric sphere respectively.

26

As seen from the plot (3.3) the bulk velocities are higher for the smaller radius. This is indicative of the fact that there can be a significant deviation from the homogeneity in the local universe. But as we move towards a larger radius, the plot converges to the red line which represents the median velocity, flatting out to zero. The significance of the bulk flow decreases as more volume is considered. The velocities approach closer to the median value, implying that over larger distances, the collective motion of dark matter particles becomes less coherent. Hence focusing on the sub-400 Mpc/h scale we can investigate the dynamics in a regime. Within this scale, we get measurable values of bulk flows that can provide insights into the matter distribution.

To see the deviation of the local density from the mean density, in fig 3.4, the density contrast is plotted. The plot shows the dimensionless density perturbation field or overdensity (see 1.1)value for the given spherical radius and chosen random center. The overdensity is widespread for smaller radii this means for the smaller spheres the measurement is highly sensitive to the environment around it. As the universe is highly nonhomogeneous on smaller scales the smaller distances show the variation according to the central point of observation. But as we approach the larger distances we approach homogeneity, the density fluctuations average out and the spheres would include all kinds of cosmic environments (voids, filaments, sheets). The value of overdensity converges to 1 here as we cover more and more volume in the box. This convergence is faster for density than that of the velocity, the following argument provides a possible explanation for this. The gravitational evolution of the dark matter particles is set forth by the initial conditions provided in the simulations. The density field and hence the gravitational field evolves faster away from the linear regime. The velocity field, influenced by the density field, is a smoother field. Because of this, velocities do not change as quickly and hence retain the initial conditions imprint longer. In other words, the velocity has a better memory of the initial conditions given than the density field and hence can trace the comic web better (Hoffman et al. (2012)).

The results obtained from both bulk flow calculations and the density contrast of the ideal spherical geometry are in accordance with our observations. The simulated volume is the replica of the universe, which supports the cosmological model suggesting homogeneity and isotropy on large scales. Hence the results serve as a sanity check for the simulated data for our arguments reinforcing our confidence in its accuracy. This ensures that the conclusions drawn from simulations can be trusted to be approximately reflective of the real universe. Therefore, studying bulk flow within this simulated environment offers valuable insights into the movements and behaviors of the actual universe.

3.2 Bulk flow in Hemispheres:

As explained previously in the section 2.4 the galaxy surveys do not have ideal spherical geometries. The survey geometry varies from survey to survey. To get an idea about the effect of the non-spherical survey geometries on the bulk flow calculation

we include simple cases in our study. Here we are considering hemispheres as one of the footprints.
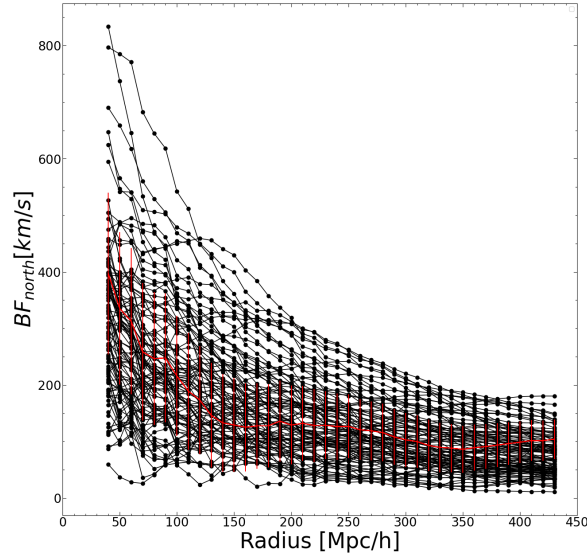
Figure 3.5: The figure gives the Bulk flow calculations for the northern hemisphere at all the random points. The axes are the same as figure 3.1. Each curve represents a randomly chosen center and each dot on the curve represents a concentric sphere which is the part of the northern half of the sphere.

The hemispherical calculations are done for the southern and the northern hemispheres. Here we defined "north" for each sphere based on the direction of the bulk flow of the whole sphere obtained from previous calculations. The procedure is explained in the section 2.4. The bulk flow is computed in the northern hemisphere, and as expected, the plot shows that the bulk flow magnitude decreases as the radius of the concentric sphere increases. Here we see a higher dispersion in the velocities compared to the calculations of the whole sphere.

For the perfectly homogeneous universe the ratio of the bulk flow in the northern hemisphere to the total bulk flow would remain 1. There will be no effect of subsampling on our measurements. To check the consistency with our assumptions we take the ratio of bulk flow in north to the total bulk flow. The blue curve shows the median of ratios for the given radii. The shaded blue area indicates the variance over the bulk flow ratios measured. Contradictory to our assumptions, from figure 3.6 we see that the ratio deviates or increases slightly as we go further in the box. There is a slight overestimation of the bulk flow for a hemispherical geometry. This overestimation might be a result of a number of factors including the biases introduced by the hemispherical geometry, and the effect of subsampling. This means that as the bulk flow is a vector quantity if the mean bulk flow is not uniformly distributed or there is a presence of inhomogeneity in the northern hemisphere this can introduce a bias. Additionally, it can be an artifact introduced due to the simulations. To check if there is a preferential directionality that could introduce a bias we extend our study to the other half of the sphere.

28
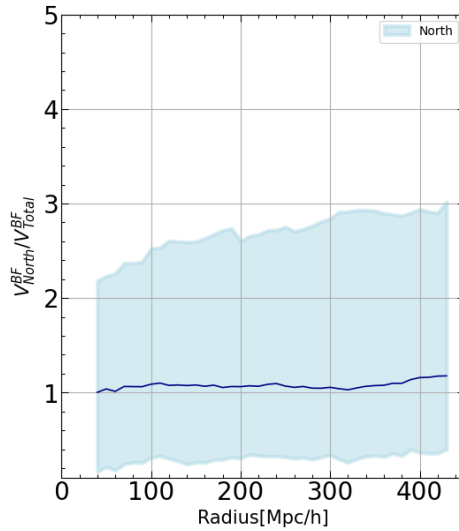
Figure 3.6: The image shows the ratio of the bulk flow in the northern hemisphere to the total bulk flow. The x-axis gives the radius and the y-axis is the value of the ratio as a function of radius. The dark blue line in the middle gives the mean value of the bulk flow for all the radii. The light blue region shows the deviation from the mean value or the error corridor for the radius.

We take half of the sphere which is pointing away from the total bulk flow vector. This is referred to as the southern hemisphere here. The bulk flow shows a consistent decrease again.
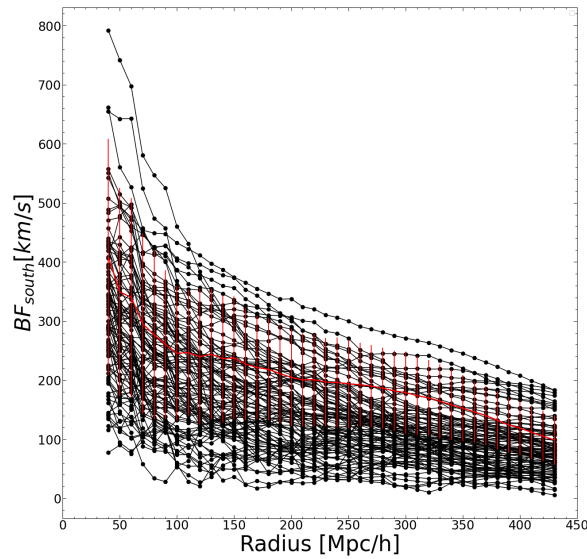
Figure 3.7: The figure gives the Bulk flow calculations for the southern hemisphere at all the random points. Each curve represents a randomly chosen center and each dot on the curve represents the hemisphere which is in the southern part. The axes are the same as the figure 3.1. The red dotted line in the middle gives the mean value.

Similar to the previous plot of the northern hemisphere, we take the ratio of bulk flow in the southern hemisphere to the total bulk flow. The bulk flow calculations in figure 3.8 show slight overestimation even with this hemisphere. The median value is the curve represented in red color. The shaded coral red area represents the

variability in the bulk flow ratio measurement. The higher variance in the upper region of the curve than the lower again emphasizes the non-gaussian nature of the velocity field. It indicates the range of values obtained from different random centers. Hence we can say that the overestimation in the magnitude of the bulk flow is present even in the direction that is opposite to the direction of the flow. In both the plots, the variance shows values more than the twice expected values. Even though, the spread in the northern hemisphere is relatively narrow, especially compared to distances < 200Mpc/h in the plot for the southern hemisphere, suggesting that the bulk flow measurements in the northern hemisphere are more consistent. Both the northern and southern hemispheres showed a ratio greater than one. This might imply that the overestimation in our measurement may not be dependent on the directionality chosen with respect to the bulk flow.
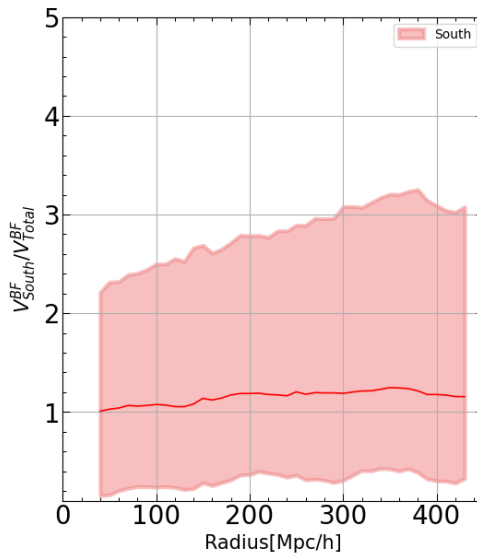
Figure 3.8: Here we see the ratio of the Bulk flow in the Southern Hemisphere to the total Bulk flow in the whole sphere. This half of the sphere is directed away from the Bulk flow. The x-axis and y-axis are similar to the above. The dark red line in the middle gives the mean which is always close to 1 and the coral region around it gives the value of the error corridor.

3.3   Bulk flow in Cones:

Another non-spherical geometry that is taken into consideration is cones with different values of angles. For this study, we consider cones of opening angles of 30° and 15°. The conical geometry allows for the measurement of bulk flow more precisely in a specific direction. The pencil beam galaxy surveys with similar geomtries are useful for the study of galaxies at various redshifts (Visbal and McQuinn (2023)). Choosing the smaller area in the sky also helps to overcome the small-scale clustering effects in galaxy distribution.
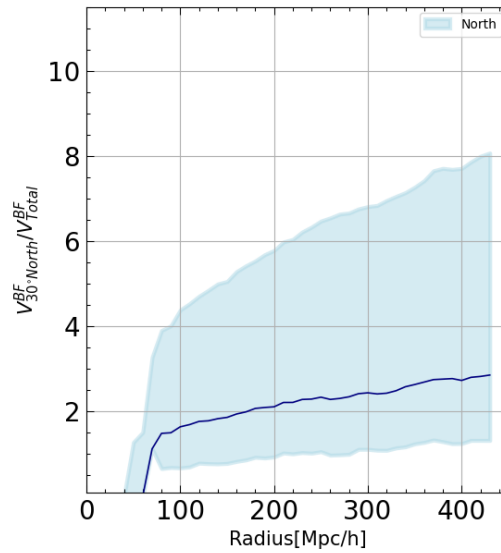
Figure 3.9: The plot shows the calculation of the bulk flow in a cone with a 30°
angle. The northern hemisphere represents a similar direction as the bulk flow. The
x and y axes are similar to the figure 3.6. The error corridor is shown in the light
blue region around it.

Here the cones are again considered in the direction of the bulk flow and away
from the direction of the bulk flow. Figure 3.9 shows the 30° cone in the direction of
the bulk flow. The cone is defined in such a way that half of the cone is taken on each
side of the bulk flow vector for the respective spheres making the opening angle of
30°. The ratio of the bulk flow in the cone to the total bulk flow again should be 1 for
a perfectly homogenous case. The median in the blue cover has values here that are
notably higher than those from the previous hemisphere plots. This suggests a more
significant flow within this conical region. The median takes the value that is higher
than twice the expected value. There is also more broadening of the shaded area
with increasing radius suggesting that the variability in the bulk flow measurements
also increases more drastically with distance from the center. But it is important to
check if this overestimation is due to the effect of subsampling

We consider the cone in the orientation in the direction which is 180° opposite to
the northern cone. Here we take the cone which is pointing away from the bulk flow
vector. Similar to the northern cone, the bulk flow in the southern cone increases
with the radius. The deviation in the highest and the lowest value of the bulk flow
also increases hence we see a larger error corridor. The initial value of the bulk flow
is zero for both the northern and southern cones. This can be attributed to the fact
that in the smallest cones, the contributions to the bulk flow from different directions
are zero as no grid points are present in these cones. As the cone encompasses larger
volumes, and thus more mass, the net bulk flow becomes nonzero and increases with
radius.
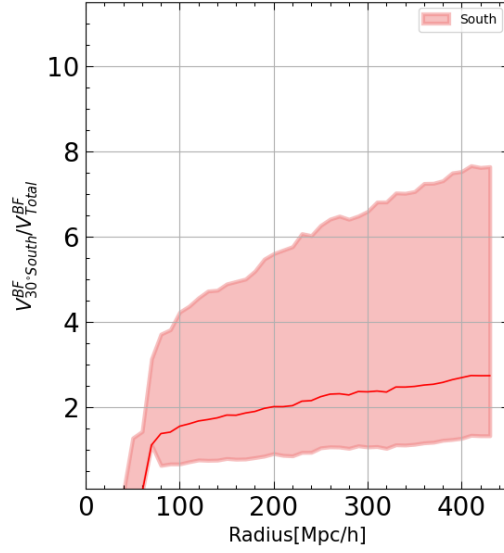
Figure 3.10: The plot shows the bulk flow of the cone pointing away from the velocity vector similar to the northern cone. The dark red line gives the mean of the ratio of the bulk flow in the cone to the total bulk flow in the cone pointing away. The axes are the same as fig 3.6. The coral region gives the value of variance around the bulk flow measurements
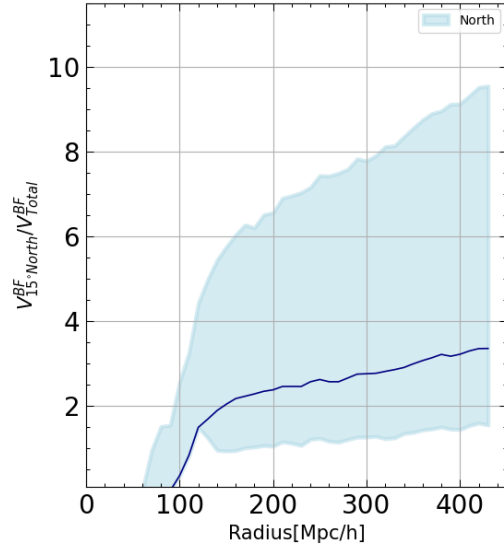
Figure 3.11: The plot shows the bulk flow estimation for a 15° cone in the direction of the bulk flow. The x and the y axes are similar to the figure 3.6. The light blue region gives the variance in the mean bulk flow which is shown with the blue line.

In conclusion, the plots for the northern and the southern 30° cone are much alike. The symmetry is observed in the trend for both the conical sections, even though there is a significant overestimation in the bulk flow for both sides.

We consider a narrower cone of 15° to focus on a smaller and potentially more coherent region of the velocity field. This may provide insights into the structure and dynamics within specific lines of sight. The plot 3.11 and the plot 3.12 show the bulk flow in the northern 15° cone to the total and in the southern 15° cone to the total bulk flow respectively. The increasing trend of bulk flow ratio with radius is

observed here as well. The values of the median shown for both directions of the cone have significant overestimation. But for the smaller cone, there is more spread or variance within the measurements The spread also appears to widen with increasing radius. The bulk flow value reaches here 8 times the expected value. This implies that the cones can perhaps drastically overestimate the bulk flow values. The initial distances for cones do not represent any value as they were null due to the conical area being empty and not having any particles to measure the bulk flow similar to the previous cones.
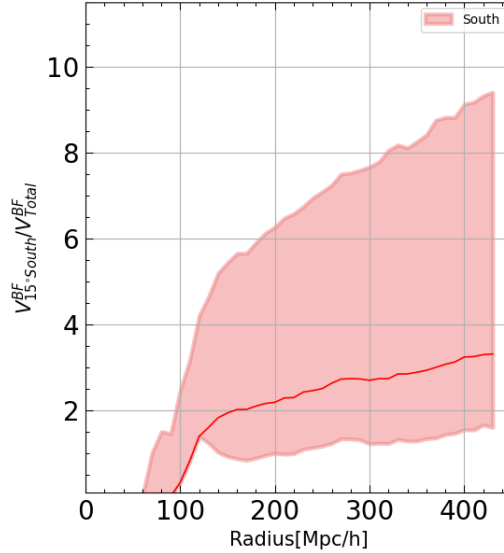
Figure 3.12: The plot shows the bulk flow for the southern cone, which is pointing away from the vector is shown. The red line shows the mean bulk flow for all the spheres and the error region is represented by the coral region. The axes are similar to the figure 3.8

3.4   Random Sampling:

To ensure that there is no biasing due to the specific chosen direction to measure the bulk flow, we make the measurements with random sampling. By choosing the random directions for the measurement of the bulk flow, we gather a robust set of measurements. The results generated with the random directions are later compared with the results obtained from specific direction measurements. This gives us an idea about the dependence of the measurements on the flow directions.

We generate 3 vector components to get the random direction for the bulk flow measurements. The sample is drawn from a Gaussian distribution peaked at zero. This ensures that the vectors in any direction are distributed around zero without any bias being chosen. This is also consistent with the assumption that on a larger scale, the universe does not have any preferred direction.
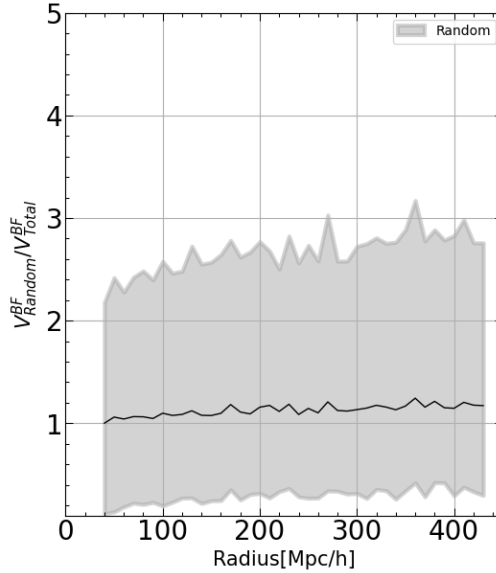
Figure 3.13: The plot shows bulk flow measurements by choosing a random velocity vector for the calculations. The x-axis represents the value of the radius of the concentric sphere that are considered. The y-axis gives the value for the ratio of the bulk flow in the random hemisphere to the total bulk flow in the entire sphere.

We see the ratio of the random hemisphere's bulk flow to the total bulk flow in the figure 3.13. The ratio hovers around 1 for most of the radius range. It appears to increase slightly as the radius approaches 400 Mpc/h. Compared to the earlier plots for the directed northern (fig 3.6) and southern (fig 3.8) hemispheres, which showed ratios consistently above 1, the random hemisphere plot starts closer to 1. The trend does not show a constant increase, unlike the previous measurements. The bulk flow measurements also show less deviation from unity here. However, the variance observed in the random hemispheres is approximately similar to the trend observed in the figure 3.6. This might suggest that when considering a specific direction (such as north or south), the bulk flow measurements revealed a stronger preferred motion. But when taken in random directions velocities do not consistently reveal such strong preferences.

To see if the strong preference in direction is only limited to the hemispherical subsampling or if the results are consistent for cones in random directions, we compare our results with the previous measurements of cones in section 3.3 from both north and south directions.
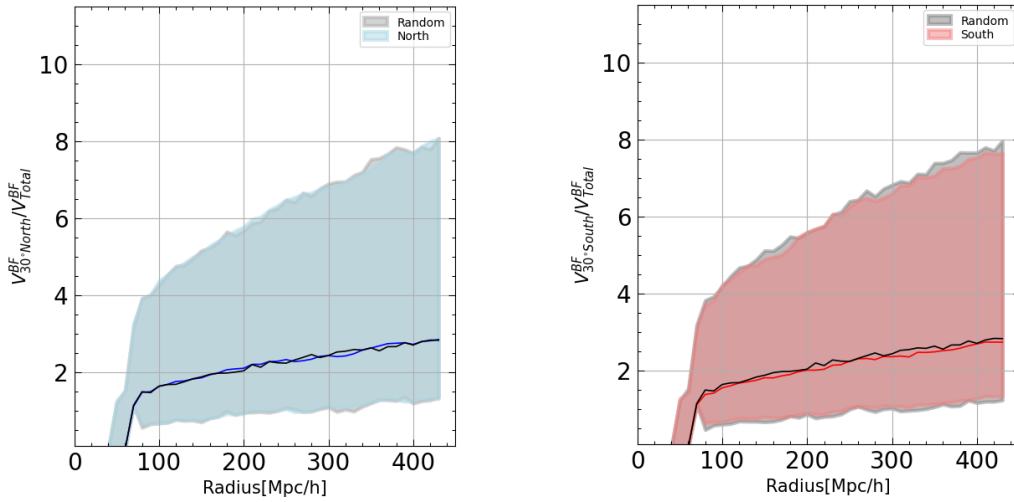
Figure 3.14: Comparision between the bulk flow measurement for a cone with opening angle 30°. The axis is the same as the figure 3.13. Blue and red lines show the mean value of bulk flow in the northern and southern parts of the cone according to the bulk flow respectively. The black line shows the cones in random directions. The shaded region shows the variance in measurements.

The left plot in 3.14 shows the comparison between the cone with an opening angle of 30° in the northern direction to the cone of the same size taken in random directions. The plot on the left shows the cone in the southern direction to the cone in the random directions. Both the plots show that a similar trend is observed for the cones in random directions as that of in or away from the flow direction. The median value of bulk flow in random cones is shown in the black colored curve in both plots. This value of bulk flow follows a similar trend as the previous conical measurement.

Similarly, the cones with the opening angle of 15° in a direction are compared to the random cones of 15°. As shown in the plot 3.15 the cones show similar results for both cases. The cone in the northern direction to the flow is shown in the left plot. This shows exact overlap with the values of the cone for the random direction measurements. But cones with both opening angles of 30° and 15° show consistent overestimation of the bulk flow as shown in figure 3.14 and figure 3.15. The measurements for the cones in the random direction show similar traces as those of the cones taken with respect to the bulk flow. The variance increases for all the cones with the increase in the distance from the origin. This implies that the bulk flow overestimation might be arising due to subsampling rather than the directionality of the measurement.
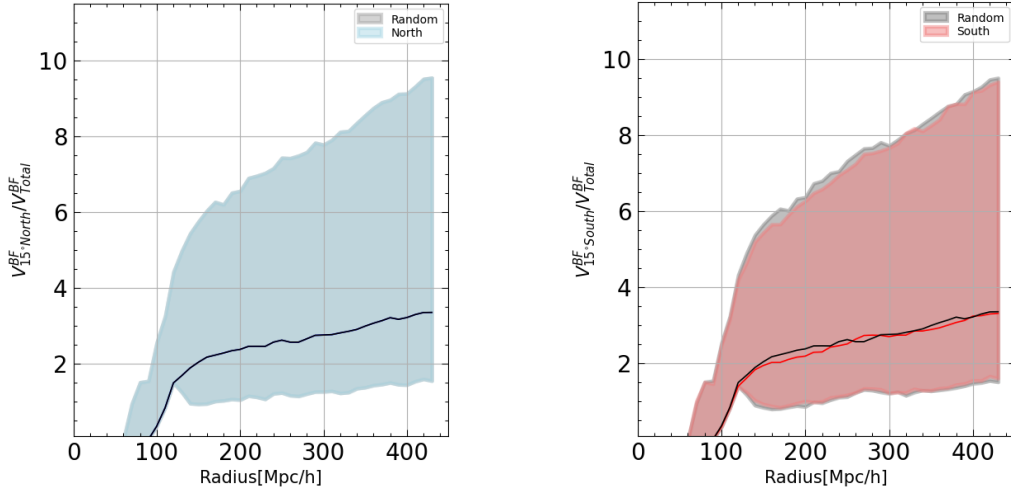
Figure 3.15: Comparision between the bulk flow measurement for a cone with opening angle 15°. The axis is the same as the figure 3.13. Blue and red lines show the mean value of bulk flow in the northern and southern parts of the cone according to the bulk flow respectively. The black line shows the cones in random directions. The shaded region shows the variance in measurements.

3.5 Comparison between the footprints
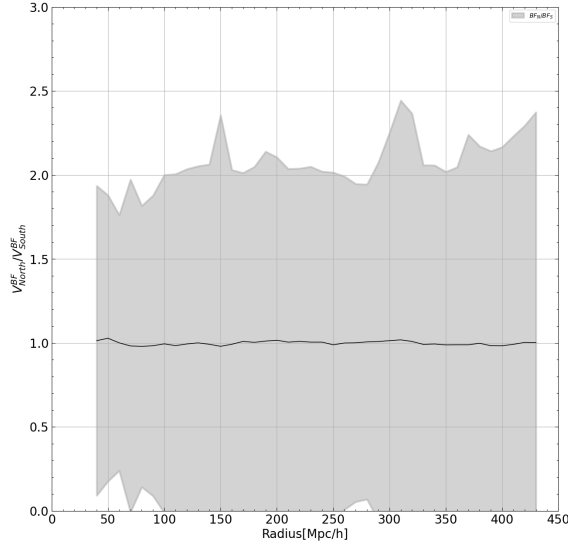
Figure 3.16: The ratio of bulk flow measured in the north hemisphere to the bulk flow in the southern hemisphere.

It is still important To ensure that minimal biasing is introduced due to the direction of the measurement of the bulk flow as the geometries taken into consideration are not ideal spheres. Hence we plot the ratio of the bulk flow in the northern to southern hemisphere as shown in the figure 3.16. The ratio is consistently 1 or very close to 1 for all the radii. The slight deviation is observed at a smaller radius which might be the result of inhomogeneity at smaller scales. The results again emphasize the fact that there is minimal to no bias introduced due to the directionality of the measurement. Even for the smaller scales or radii where we might expect higher

dispersion in the bulk flow values a similar result is observed. Hence we can say that the bulk flow between the 2 opposite hemispheres averages out, especially for larger radii. Therefore there is no preferred direction for measurements that introduce the bias.
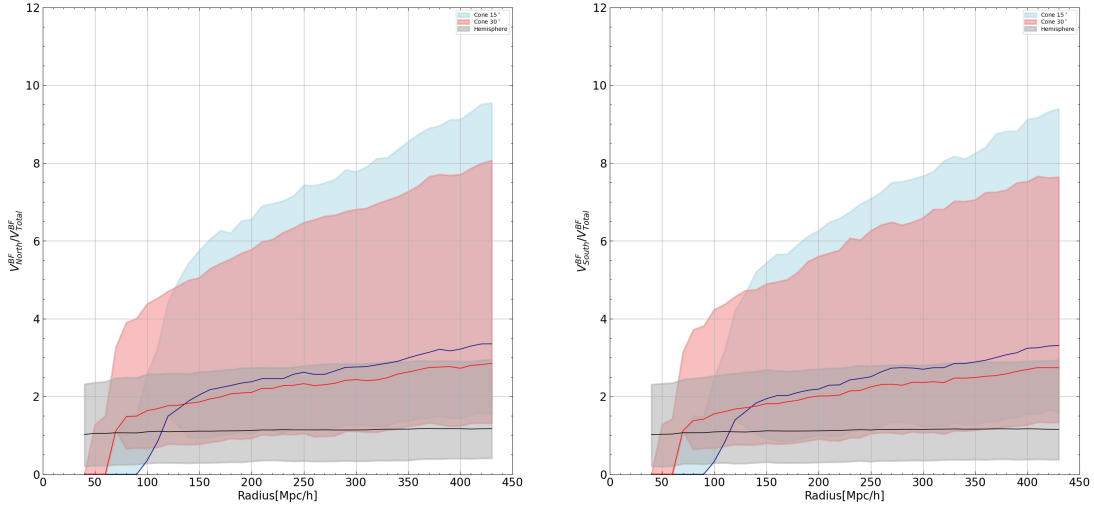
Figure 3.17: Comparision between different footprints' bulk flow measurements. The blue, red, and black line shows the mean of bulk flows in cones of 15°, 30°, and hemisphere respectively.

After confirming the idea that the bias is not introduced due to the direction we compare the different subsamples of the bulk flow measurements. The plot (3.17) shows the comparison of different subsamples. The left panel has the bulk flow measurements for all three subsamples namely hemisphere, cone of 30°, cone of 15° in the direction of the flow. The right panel shows the comparison between the subsamples away from the direction of the flow or the southern part. The black line in both plots shows the velocity measurements for the hemispherical subsampling. The blue and the red line shows a cone of 15° and a cone of 30° respectively. After comparing the bulk flow measurements of the different footprints we see that the undersampling effects introduce overestimation. From the figure 3.17 we see that the deviation from unity increases as we consider the narrow area for bulk flow calculations. From our results, we can conclude that the bulk flow ratio shows the least deviation for the hemispheres, a higher deviation for the 30° cone, and the highest deviation for the 15° cone. The results are affected by the sampling effects more than the directionality of the measurements. As we take the bulk flow measurements for narrow cones more overestimation is observed. This can be the result of undersampling due to the narrow geometries.

Chapter 4

Disussion and Summary

In this thesis, we have discussed the observational effects on bulk flow measurements. Dark matter-only simulations are used for understanding the dynamics of the real universe matter density. The box has comoving coordinates hence the velocity components here add to the peculiar velocities. The average of these peculiar velocities on particles for a large spherical region centered on the observer is taken to calculate the bulk flow. Different sampling geometries have been used on the simulated data for the measurements of the bulk flow. The following results are obtained,

	North	South	Random
Direction	in the direction of bulk flow	away from the direction of the bulk flow	randomly oriented
Sphere	slight overestimation	slight overestimation	inconsistent/no overestimation
30° cone	high overestimation	high overestimation	high overestimation
15° cone	very high overestimation	very high overestimation	very high overestimation

Table 4.1: Bulk flow estimations for different subsamples

To mimic the different geometries of the galaxy surveys, we calculate the bulk flow for complete spheres, hemispheres, and cones. To avoid biases due to a particular direction we also measure the bulk flow in the random directions. To study the variance in measurements we take multiple observer origins in the box. The geometries are defined around these origins for the measurement of the bulk flow.

The results show biasing toward measuring the larger bulk flow magnitudes than the underlying bulk flows. As the survey geometry becomes narrower higher biasing is observed with most narrow cones showing the highest overestimation in the value. This implies that the estimated values of the bulk flow measurements which use a small number of peculiar velocities are biased due to undersampling effects in a way that the bulk flow values are overestimated. From the plot 3.17 we see that not only is the bulk flow overestimated for the narrower geometry but the variance over the value of the estimated bulk flow also increases. This variance and overestimation increases as a function of radius.

The possible explanation for this explained in the Andersen et al. (2016) is as follows. Considering a large volume in the universe where the galaxies obey the

cosmological principle. Hence the total velocities of all N galaxies in this volume yield a bulk flow magnitude of exactly zero. This must be true even if only line-of-sight velocities are observed. Then from this volume only n < N galaxy velocities are considered the bulk flow measurement will give a non-zero value this time. As the magnitude is always positive we always estimate some non-zero positive number. Even after taking into consideration a sample of some other n < N galaxies the argument still remains valid. Only if we consider a number of galaxies such that n ≡ N then only we can get a value of bulk flow that is closer to zero.

4.1   Conclusion

The thesis provides significant insights into the peculiar velocity fields, offering a deeper understanding of the bulk flows. The results bring to the forefront the effect of different geometries of survey catalogs on bulk flow measurements. We studied the bulk flow measurements for different sampling geometries and we found:

- As expected the bulk flow reduces and converges to zero when we move towards the larger scales. This is consistent for all the geometries.

- The northern and the southern hemispherical geomtries show a slight overestimation in the bulk flow.

- Cones of 30° and 15° also show overestimation in the bulk flow measurements.

- As we take into consideration the narrower geometry we observe higher overestimation in the bulk flow values.

- Similar results are obtained for the cones and hemispheres taken in random directions implying the overestimation is not the effect of direction of measurement.

- The bulk flow overestimation is maximum for the smallest opening angle of 15° and the least for the hemispheres.

- This might explain the measurement of the higher bulk flow values than expected in the Λ-CDM cosmologies.

From these results, we can conclude that undersampling effects introduce strong bias in the bulk flow measurements. For non-spherical survey geometries of the peculiar velocity catalogs of galaxies, this might give the overestimated value of the bulk flow. While considering the bulk flow measurements from such survey geometries it is important to take into account these overestimations.

Chapter 5

Future direction

Even while there is remarkable agreement between simulations and observations the ongoing tensions suggest that flat Λ-CDM based on Planck (Planck Collaboration and Aghanim (2020)) values may not ultimately be the correct model (Riess et al. (2019)). In recent years, great progress has been made to address the discrepancy (Di Valentino et al. (2021)) a ∼ 10% discrepancy in the value of the Hubble constant as determined from local measurements still persists.

The Cosmic Microwave Background(CMB) dipole is the motion of the local group of galaxies relative to the CMB rest frame. The dipole is linked to the anomalies in CMB (Naselsky et al. (2011)) which challenge the inflationary Λ-CDM model. Additionally, the attempts to recover CMB dipole from late universe sources such as radio galaxies have shown that there is agreement with the direction recovered but not with the magnitude (Blake (2002)). Similar findings have also been observed from studies of apparent magnitudes of type Ia supernovae (SN) (Krishnan et al. (2022)) and QSOs (Secrest et al. (2021)). It is important to note that all these results are from the partial sky surveys.

From our study, we see that the observational effects introduce bias in our measurements of the peculiar velocities. The peculiar velocities of the galaxies contribute to the bulk flow. We specifically compare the bulk flow measurements with the theoretical predictions. In galaxy surveys, the peculiar velocities are approximated to get the bulk flow that would occur around the sphere of the observer. But when the survey geometries are non-spherical the methods for bulk flow estimation overestimate the values.

The bulk flow represents the peculiar motion of galaxies in addition to their expansion with the Hubble flow. Discrepancies in the bulk flow measurements might affect the overall H_0 measurement. This might provide an explanation for the larger values of H_0 measurements in the direction of CMB dipole observed, among many others by the work in Krishnan et al. (2022). We would like to work towards understanding the large-scale velocity fields in the local universe taking into account the overestimations observed in our measurements.

Bibliography

Andersen, P., Davis, T. M., and Howlett, C. (2016). Cosmology with peculiar velocities: observational effects. , 463(4):4083–4092.

Angulo, R. E. and Hahn, O. (2022). Large-scale dark matter simulations. *Living Reviews in Computational Astrophysics*, 8(1):1.

Bernardeau, F., Colombi, S., Gaztañaga, E., and Scoccimarro, R. (2002). Large-scale structure of the Universe and cosmological perturbation theory. , 367(1-3):1–248.

Blake, C., W. J. A. (2002). velocity dipole in the distribution of radio galaxies. *Nature*.

Colless, M. e. a. (2001). The 2dF Galaxy Redshift Survey: spectra and redshifts. , 328(4):1039–1063.

Di Valentino, E., Mena, O., Pan, S., Visinelli, L., Yang, W., Melchiorri, A., Mota, D. F., Riess, A. G., and Silk, J. (2021). In the realm of the Hubble tension-a review of solutions. *Classical and Quantum Gravity*, 38(15):153001.

D'Inverno, R. (1992). *Introducing Einstein's Relativity*. Oxford University Press.

Einstein, A. (1915). *Sitzungsberichte der Preußischen Akademie der Wissenschaften 1,*, page 831.

Ellis, G. F. R. and van Elst, H. (1999). Cosmological Models (Cargèse lectures 1998). In Lachièze-Rey, M., editor, *Theoretical and Observational Cosmology*, volume 541 of *NATO Advanced Study Institute (ASI) Series C*, pages 1–116.

Freedman, W. L., Madore, B. F., Gibson, B. K., Ferrarese, L., Kelson, D. D., Sakai, S., Mould, J. R., Kennicutt, Robert C., J., Ford, H. C., Graham, J. A., Huchra, J. P., Hughes, S. M. G., Illingworth, G. D., Macri, L. M., and Stetson, P. B. (2001). Final Results from the Hubble Space Telescope Key Project to Measure the Hubble Constant. , 553(1):47–72.

Friedman, A. (1922). Über die krümmung des raumes. *Zeitschrift für Physik*, 10(1):377–386.

Han, M. and Mould, J. (1990). The Velocity Field in the Local Supercluster. , page 448.

Hoffman, Y., Metuki, O., Yepes, G., Gottlöber, S., Forero-Romero, J. E., Libeskind, N. I., and Knebe, A. (2012). A kinematic classification of the cosmic web. , 425(3):2049–2057.

Howlett, C. e. a. (2022). The Sloan Digital Sky Survey peculiar velocity catalogue. , 515(1):953–976.

Hubble, E. (1929). A Relation Between Distance and Radial Velocity Among Extra-Galactic Nebulae. In *Proceedings of the National Academy of Science*, pages 168–173.

Klypin, A., Yepes, G., Gottlöber, S., Prada, F., and Heß, S. (2016). MultiDark simulations: the story of dark matter halo concentrations and density profiles. , 457(4):4340–4359.

Krishnan, C., Mohayaee, R., Colgáin, E. Ó., Sheikh-Jabbari, M. M., and Yin, L. (2022). Hints of FLRW breakdown from supernovae. , 105(6):063514.

Laureijs, R. e. (2011). Euclid Definition Study Report. *arXiv e-prints*, page arXiv:1110.3193.

Lavaux, G. and Hudson, M. J. (2011). The 2M++ galaxy redshift catalogue. , 416(4):2840–2856.

Lilje, P. B. e. a. (1986). The Tidal Velocity Field in the Local Supercluster. , 307:91.

Naselsky, P., Zhao, W., Kim, J., and Chen, S. (2011). Is the CMB asymmetry due to the kinematic dipole? *arXiv e-prints*, page arXiv:1108.4376.

Peter Coles and Francesco Lucchin (2002). *Cosmology:The Origin and Evolution of Cosmic Structure*. John Wiley Sons, Ltd.

Pfrommer, C. (2022). lecture notes on, Modern Computational Astrophysics: Concepts and Applications.

Planck Collaboration and Aghanim, N. e. a. (2020). Planck 2018 results. VI. Cosmological parameters. , 641:A6.

Riess, A. G., Casertano, S., Yuan, W., Macri, L. M., and Scolnic, D. (2019). Large Magellanic Cloud Cepheid Standards Provide a 1% Foundation for the Determination of the Hubble Constant and Stronger Evidence for Physics beyond ΛCDM. , 876(1):85.

Sarkar, P., Yadav, J., Pandey, B., and Bharadwaj, S. (2009). The scale of homogeneity of the galaxy distribution in SDSS DR6. , 399(1):L128–L131.

Schechter, P. L. e. a. (1981). The Velocity Field in the Local Supercluster. In *Bulletin of the American Astronomical Society*, volume 13, page 799.

Secrest, N. J., von Hausegger, S., Rameez, M., Mohayaee, R., Sarkar, S., and Colin, J. (2021). A test of the cosmological principle with quasars. *The Astrophysical Journal Letters*, 908(2):L51.

Tully, R. B., Courtois, H. M., and Sorce, J. G. (2016). Cosmicflows-3. , 152(2):50.

Tully, R. B. e. a. (2016). Cosmicflows-3. , 152(2):50.

Visbal, E. and McQuinn, M. (2023). Cross Correlation of Pencil-beam Galaxy Surveys and Line-intensity Maps: An Application of the James Webb Space Telescope. , 956(2):84.

Vogelsberger, M., Zavala, J., Cyr-Racine, F.-Y., Pfrommer, C., Bringmann, T., and Sigurdson, K. (2016). ETHOS - an effective theory of structure formation: dark matter physics as a possible explanation of the small-scale CDM problems. , 460(2):1399–1416.

Wang, H., Mo, H. J., Yang, X., Zhang, Y., Shi, J., Jing, Y. P., Liu, C., Li, S., Kang, X., and Gao, Y. (2016). ELUCID - Exploring the Local Universe with ReConstructed Initial Density Field III: Constrained Simulation in the SDSS Volume. , 831(2):164.

Wojtak, R. e. a. (2014). Cosmic variance of the local Hubble flow in large-scale cosmological simulations. , 438(2):1805–1812.

2

Appendix A

Analysis of Bulk Flow

A.1 256^3 point grid

The bulk flow evaluation on a 256^3 grid
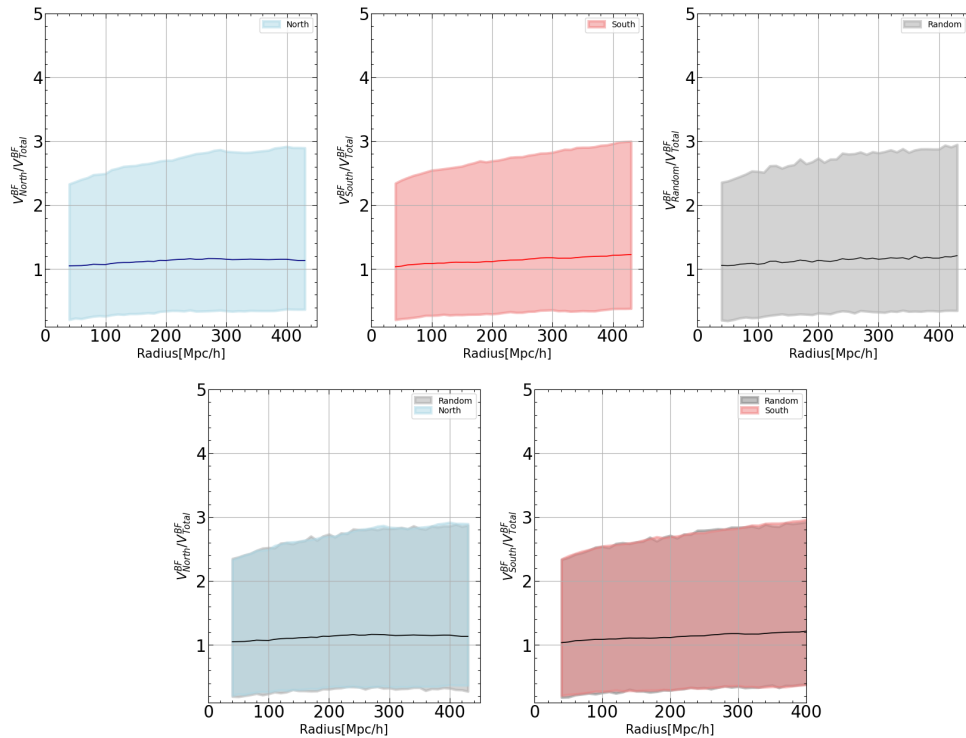
Figure A.1: Bulk flow calculations for hemispheres using 256^3 grid, axes are similar to the plot 3.5. The top leftmost plot shows bulk flow in the ratio of the northern hemisphere to the total bulk flow, the top middle plot shows bulk flow in the southern hemisphere to the total bulk flow, and the top right-most shows the bulk flow in the random hemisphere to the total bulk flow. The two plots at the bottom are a comparison of the north hemisphere to the random hemisphere (left) and a comparison of the random hemisphere to the southern hemisphere
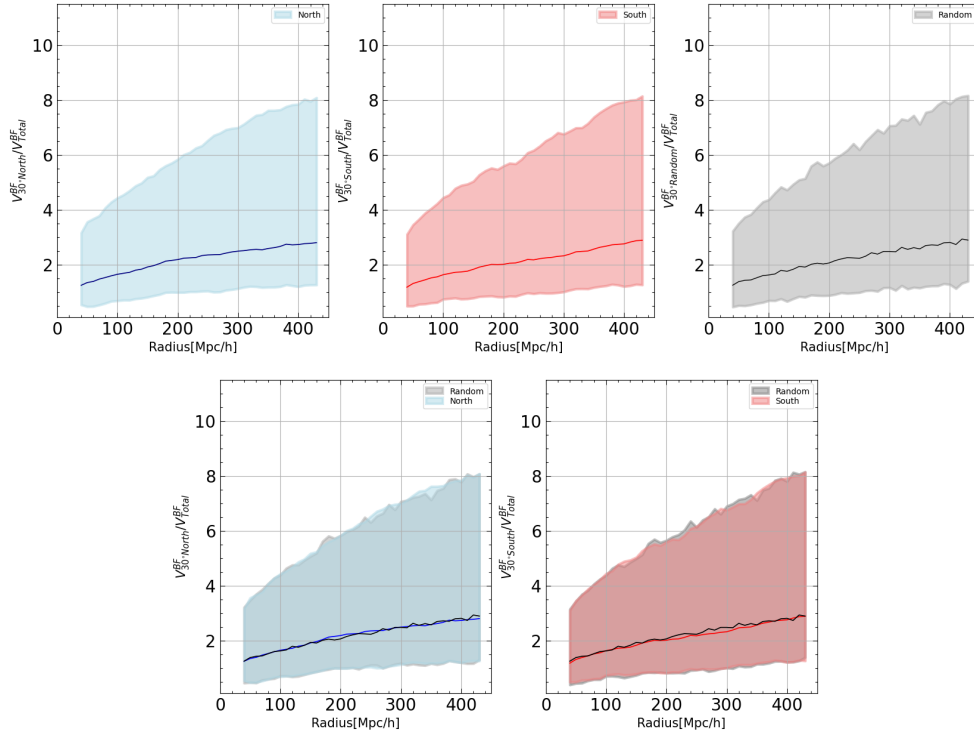
Figure A.2: Bulk flow calculations for cones with an opening angle of 30° using 256^3 grid, axes are similar to the plot 3.5. The top leftmost plot shows bulk flow in the ratio of the northern cone to the total bulk flow, the top middle plot shows bulk flow in the cone to the total bulk flow, and the top right-most shows the bulk flow of cones in a random direction to the total bulk flow. The two plots at the bottom are a comparison of the north cone to the random cone (left) and a comparison of the cones in the south to the random cone (right).
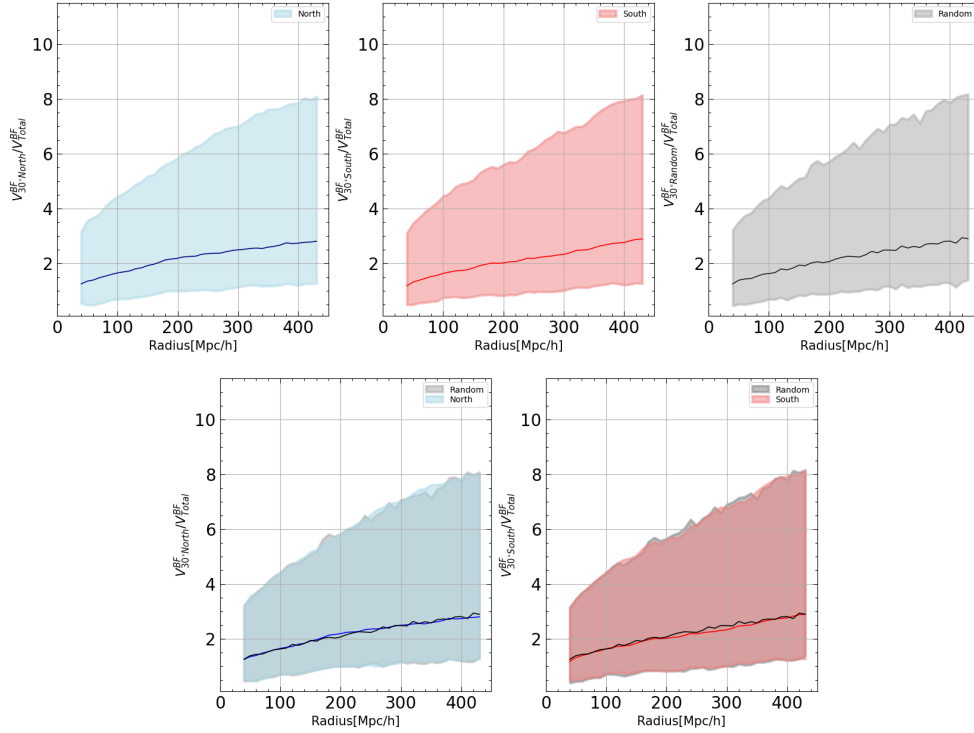
Figure A.3: Bulk flow calculations for cones with an opening angle of 15° using 256^3 grid, axes are similar to the plot 3.5. The order of plots is similar to A.2.

A.2 Halo catalog

Bulk flow analysis using the Halo catalog for the 128^3 grid and 256^3 grid.
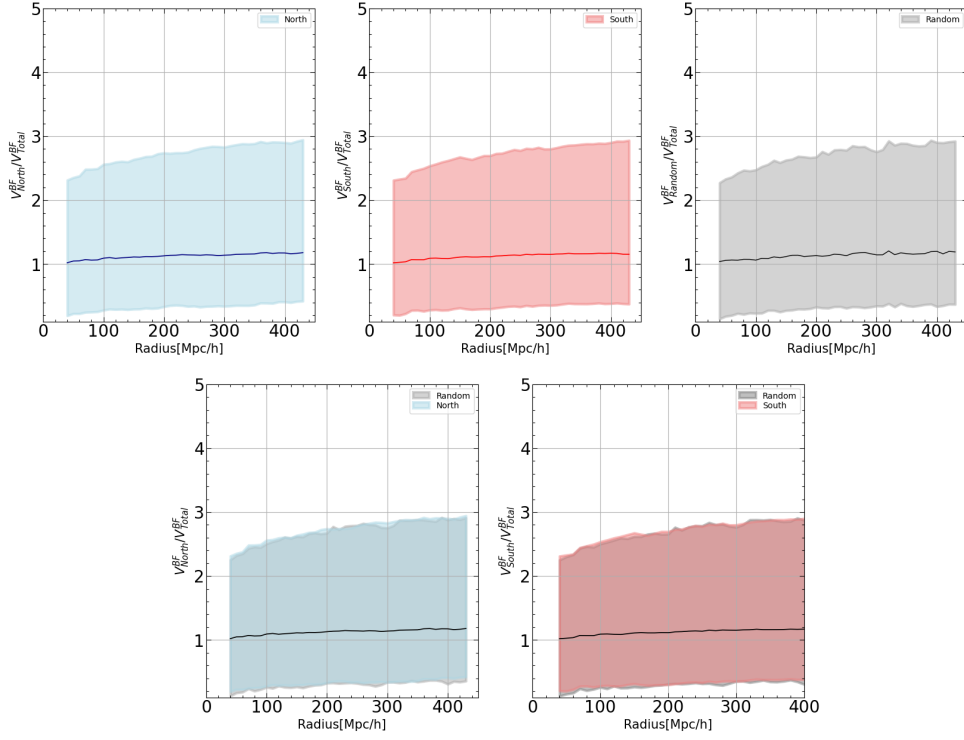
Figure A.4: Bulk flow calculations for hemispheres using 128^3 grid, using the halo catalog, axes are similar to the plot 3.5. The order of plots is similar to A.1.
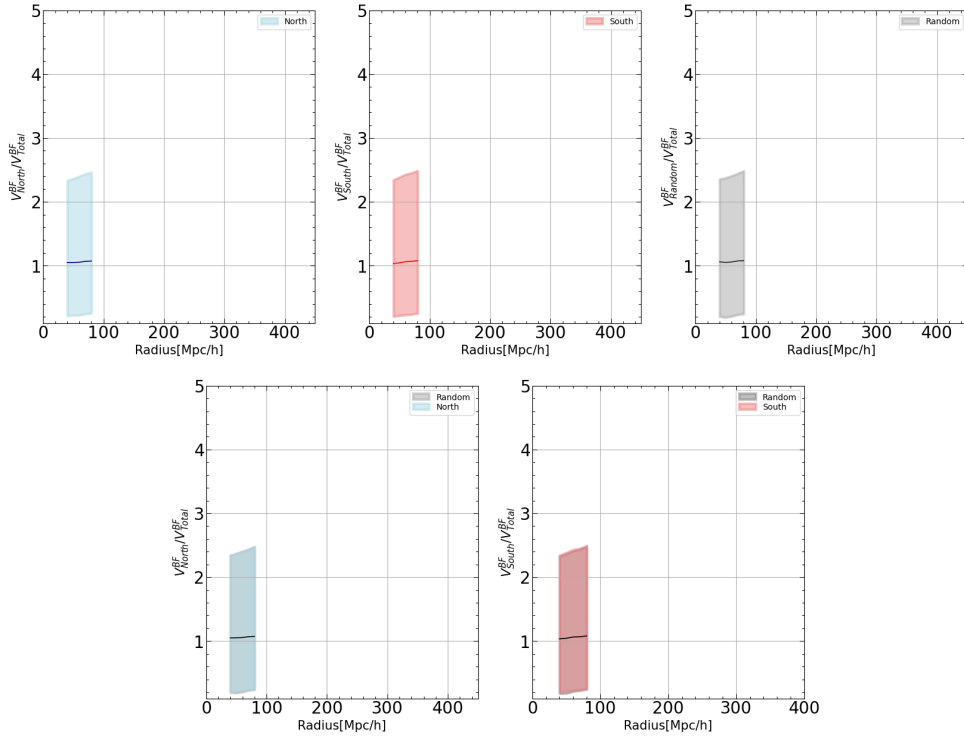
Figure A.5: Bulk flow calculations for hemispheres using 256^3 grid, using the halo catalog, axes are similar to the plot 3.5. The order of plots is similar to A.1.

List of Figures